Chronic lysosome damage boosts interferon responses to Palbociclib dependent upon the mitochondrion

Mihaela Bozic[1], Tian En Lim[1], Carla Salomó-Coll[1], Arianna Karageorgiou[1], Alain J. Kemp[1], Katie Winnington-Ingram[1], Laura Murphy[2], Ashish Dhir[2,3], Ann Wheeler[2], Natalia Jimenez-Moreno[1], Simon Wilkinson[1*]

[1]Cancer Research UK Scotland Centre, Institute of Genetics and Cancer, University of Edinburgh, Edinburgh EH4 2XR, UK

[2]MRC Human Genetics Unit, Institute of Genetics and Cancer, University of Edinburgh, Edinburgh EH4 2XU, UK

[3]Current address: 4BASEBIO DISCOVERY LIMITED, 25 Norman Way, Over, Cambridge, Cambridgeshire, England, CB24 5QE, UK

[*]Corresponding author, s.wilkinson@ed.ac.uk

Keywords: lysosome; Palbociclib; lysophagy; immunogenic nucleic acid; interferons; autophagy

19 ## Abstract

20 Acute lysosome damage triggers the endolysosome damage response (ELDR) in order to co-ordinate
21 vesicle repair or removal by autophagy (lysophagy). However, it is unclear whether persistent damage,
22 as occurs after chronic challenge to lysosome integrity, triggers wider cellular responses. Here, we
23 show that longitudinal treatment with a lysosomotropic cancer therapeutic, the CDK4/6 inhibitor
24 Palbociclib, invokes chronic lysosome damage in breast and lung cancer cells. Autophagy ameliorates
25 but does not avert this phenotype, which persists over days. Damaged lysosomes form contacts with
26 mitochondria, which correlates with mitochondrial stress and cytosolic efflux of immunostimulatory
27 mitochondrial nucleic acids. Importantly, mitochondrial nucleic acid release is necessary for the anti-
28 cancer interferon response to Palbociclib. In conclusion, chronic lysosome damage rewires cellular
29 signalling responses in a mitochondrion-dependent manner and this effect should be considered when
30 assessing the cellular actions of cancer therapeutics.

31

Summary statement

Bozic *et al* suggest that lysosome damage can trigger interferon responses dependent upon mitochondrial release of immunogenic nucleic acid. This is associated with damaged lysosome-mitochondrion contacts and is prevented by autophagy.

Introduction

Lysosomes are single membrane-bound hydrolytic organelles that act at the termini of endocytic and autophagic pathways [1]. Although rupture of pathogen-containing phagolysosomes is a feature of some infections [2], it is also well established that, in a sterile context, widespread loss of integrity of lysosomes can result in toxic leakage of hydrolytic proteases to the cytoplasm and subsequent cell death [3]. However, acute, sublethal loss of lysosome membrane integrity typically induces the endolysosome damage response (ELDR), a collective term for pathways facilitating membrane stabilisation and repair [4-6], new lysosome biogenesis [7] or lysophagy [8], the latter being the process of selective degradation of the damaged lysosome via autophagy [9]. Lysophagy requires evolutionarily-conserved core autophagy proteins that facilitate generation of nascent autophagosome vesicles and the concurrent sequestration of damaged lysosome cargo therein [10,11]. Mature autophagosomes fuse with healthy lysosomes to facilitate degradation of sequestered cargo. Damaged lysosomes are initially recognised for degradation via “eat-me” signals [8,12]. These include recruitment of galectin proteins, for instance Galectin 8 (GAL8) [2,13], to glycosylated lysosomal membrane proteins, and conjugation of polyubiquitin chains to lysosomal proteins [14,15].

Mechanistically, acute damage to lysosomes leads to galectin- and polyubiquitin-mediated recruitment of molecules that mediate lysophagy [2,7,13,16-21], in particular adaptors that bind directly to ATG8 (LC3/GABARAP) proteins conjugated to nascent autophagosome membranes [22] and which also recruit additional factors upstream of ATG8 conjugation [23-26]. Indeed, deletion of *ATG5* (Autophagy Related 5), which prevents ATG8 conjugation to autophagosomal (and lysosomal) membranes, is effective in stabilising damaged lysosomes by ablating lysophagy and also by compromising ATG8-mediated recruitment of repair factors [27,28]. Importantly, the removal and repair responses described above are engaged acutely, within minutes of lysosomal damage.

Notably, while extensive lysosome damage provokes cell death, linked to neurodegeneration [1,3] and disorders in other tissues such as kidney [9], it is known that lysosome damage *per se* is not necessarily lethal to cells [29], and the broader cellular consequences of chronic — yet sublethal — damage are unclear. This is particularly true in the context where the acute restorative ELDR functions, such as those dependent upon *ATG5*, are overwhelmed. Recent data indicate that programmed signalling responses to lysosome damage may exist [13]. For instance, lysosome rupture triggers RNA stress granule formation via Protein Kinase R (PKR) activation, which may maintain cell survival, over at least

the first four hours of lysosomal challenge [30,31]. However, on the whole, mechanistic studies have focussed heavily on acute damage after treatment with tool compounds, such as the membrane lytic peptide L-Leucyl-L-Leucine methyl ester (LLOMe) [9]. Importantly, numerous cancer therapeutics accumulate within lysosomes in either the cancer cells or other cell types. Generally, this phenomenon is viewed as detracting from therapeutic output by sequestering molecules from their primary targets. Nonetheless, it is possible that this may be consequential for the mechanism of the drugs. For instance, exposure of primary myeloid cells with lysosomotropic tyrosine kinase inhibitors may trigger lysosome damage and inflammasome activation, potentially contributing to treatment efficacy [32].

Palbociclib (Pb) is an important anti-cancer drug that is sequestered from its enzymatic target, the cell-cycle progression kinase CDK4/6 (cyclin-dependent kinase 4/6), due to lysosomal trapping [33]. Strikingly, in addition to cell-cycle inhibition, Palbociclib also engages an anti-tumoural interferon response [34-36]. Signalling occurs via detection of immunostimulatory moieties, purportedly from nuclear-derived double-stranded (ds) RNA [37], by cytosolic pattern recognition receptors (PRRs) [38], including RIG-I (retinoic-acid inducible gene 1) working in tandem with MAVS (mitochondrial antiviral signaling protein) [39-42]. This action of Palbociclib has been shown to drive anti-tumour immunity [34]. Indeed, discovering triggers and mechanisms of sterile interferon responses via PRRs is an important research goal in cancer therapy [43,44]. Other potential triggers could include exogenous DNA, nuclear DNA, and mitochondrial DNA or dsRNA [45-48].

Here, we reveal a link between chronic lysosome damage and interferon signalling. We show that chronic lysosome damage can be provoked by Palbociclib, independently of CDK4/6, as well as the tool compound LLOMe. Chronic lysosome damage results in persistent interorganellar contacts between ruptured lysosomes and mitochondria. Lysosome damage is associated with stress responses within mitochondria and, ultimately, accumulation of immunostimulatory mitochondrial nucleic acid in the cytosol, which we show is a requisite event for productive interferon responses. However, in the case of Palbociclib the interferon responses are synergistically facilitated by concomitant CDK4/6 inhibition. Overall, our data show that mitochondria act as priming hubs in triggering of sterile interferon responses associated with chronic lysosome damage. This molecular mechanism has implications for understanding of — and for amelioration or enhancement of — the cellular response to various chronic insults, including cancer therapeutics.

101 ## Results

102 **Palbociclib induces chronic lysosome damage and ELDR**

103 We hypothesised that Palbociclib (Pb) might trigger lysophagy since it accumulates in lysosomes and
104 causes swelling [33], i.e., potentially indicative of lysosome damage. Importantly, cancer treatments are
105 applied chronically, over days and weeks, rather than on the acute minute-to-hour scales typically
106 employed in lysophagy studies. We thus examined engagement of lysophagy flux by 24 h treatment
107 with Pb, alongside the established lysosome-damaging compound LLOMe; these assays were
108 performed using a new, sensitive reporter consisting of GAL8 fused to the C-terminus of SRAI (signal-
109 retaining autophagy indicator, Fig. 1A) [49,50]. Similar to LLOMe, Pb treatment was discovered to trigger
110 lysophagy flux in A549 lung and MCF7 breast cancer cells (Figs. 1B, C, S1). Corroborating this, we also
111 tested GAL8 fused to the conventional mRFP-GFP autophagy flux probe, and enumerated discrete
112 individual autolysosomes containing damaged lysosome remnants ($mRFP^+$ GFP^- galectolysosomes,
113 wherein the acidic lysosome environment quenches the GFP signal, Fig. 1D, E). Again, these were
114 induced by Pb treatment; additionally, consistent with elevated lysophagy flux, they were dependent
115 upon *ATG5* (non-targeted wild-type, NT, compared with Δ*ATG5* cells, Fig. 1D, E).

116

117 Next, we examined the steady-state abundance of damaged lysosomes over both acute and chronic
118 treatment regimens. YFP-GAL8 foci, indicative of undegraded and unrepaired damaged lysosomes,
119 were observed in response to chronic 48 h Pb treatment in A549 cells (Fig. 2A), in particular within the
120 autophagy-deficient Δ*ATG5* cells. These YFP-GAL8 foci co-stained with the lysosomal maker lysosomal-
121 associated membrane protein 2 (LAMP2), as expected (Fig. 2B). Quantifying these foci at multiple time
122 points of treatment, it was observed that treatment with Pb provoked a biphasic response in wild-
123 type A549 (NT) cells; a single dose invoked YFP-GAL8 foci accumulation within 1 h, peaking at 24 h,
124 but then resolving by 48 h (Fig. 2C), whereas in Δ*ATG5* cells damaged lysosomes persisted at 48 h. A
125 similar trend was observed for single dose LLOMe treatment, although the peak abundance of
126 damaged lysosomes was observed earlier and, while still evident at 8 h, was completely resolved by
127 24 h in wild-type (NT) cells (Fig. 2D). Broadly similar responses to Pb and LLOMe were seen in wild-
128 type MCF7 cells, although Palbociclib-induced lysosome damage was still evident at 48 h here,
129 suggesting a lower capacity than A549 cells for *ATG5*-dependent damage resolution (Fig. 2E, F). Finally,
130 the lysosome damaging effect of Pb was observed to be independent of its nucleocytoplasmic targets,
131 CDK4 and CDK6; A549 Δ*ATG5* cells were stably knocked out for CDK4 (Δ*CDK4*) and then CDK6 was
132 acutely knocked out (g*CDK6*), immediately prior to Pb treatment (in order to avoid confounding

133 senescence engaged by double knockout) (Fig. 2G), yet this did not alter YFP-GAL8 focus induction by
134 Pb (Fig. 2H).

135

136 Considering the above data together, we propose a new role for Pb in inducing chronic lysosome
137 damage and lysophagy, independently of its primary target, CDK4/6. Moreover, the stabilisation of
138 damaged lysosomes in A549 Δ*ATG5* cells, after single treatment with Pb, provides a facile
139 experimental setting for unpicking the events downstream of chronic lysosome damage.

140

141 **Damaged lysosomes associate with mitochondria**

142 Under basal conditions, unperturbed lysosomes form transient interorganellar contacts with
143 mitochondria [51]. Given reports that Pb may also perturb mitochondrial physiology [52], we hypothesised
144 that damaged lysosomes could associate with mitochondria. To explore this, we first performed
145 transmission electron microscopy (TEM) of Pb-treated A549 cells (Fig. 3A). Here, particularly in *ATG5*-
146 deficient cells, the presence of swollen, electron-lucent lysosomes was apparent when compared to
147 untreated controls. The increased mass of the lysosomal compartment was corroborated by flow
148 cytometry with Lysotracker Red (LTR) (Fig. 3B) and morphometric quantification of the TEM images
149 (Fig. 3C). The latter analysis also revealed that interorganellar contacts between lysosomes and the
150 mitochondrial network were increased (Fig. 3D, see also arrowheads in zoom panel in Fig. 3A). Thus,
151 we inferred that swollen lysosomes induced by Pb were in contact with the mitochondrial network,
152 although it was not possible to determine if any of these were damaged *per se*. Thus, next, using super-
153 resolution immunofluorescence microscopy, we determined that YFP-GAL8 lysosome foci induced by
154 Pb were indeed associated with — and enwrapped — the mitochondrial network (demarcated by
155 Translocase of Outer Mitochondrial Membrane, TOM20, Fig. 3E, Movie S1). The non-random nature
156 of this association was quantified by analysing the distances of YFP-GAL8 foci from the outer surface
157 of the mitochondrial network and comparing to those observed after YFP-GAL8 foci were
158 computationally shuffled to random positions within the cytoplasmic space (Fig. 3F). Finally, foci
159 dynamics were observed by super-resolution radial fluctuation (SRRF) time-lapse microscopy (Fig. 3G,
160 Movies S2, 3). YFP-GAL8 structures persistently resided along the mitochondrial network, with no or
161 few dissociation events observed over recording times of 10 minutes (Fig. 3G, Movies S2, 3). Taking
162 the above data together, we conclude that chronic damage by Pb results in ruptured lysosomes — or
163 fragments thereof — becoming stably associated with the mitochondrial network.

164

165 **Lysosome damage triggers stereotypical markers of mitochondrial nucleic acid stress**

166 Recently, nucleic acid efflux from the mitochondrion has been described as a signal that triggers
167 interferon responses. This phenomenon frequently correlates with evidence of mitochondrial nucleic
168 acid stress, as visualised by the aggregation of mitochondrial genome nucleoids [53-55]. We hypothesised
169 that contact between damaged lysosomes and mitochondria might be associated with such
170 mitochondrial nucleic acid stress. Indeed, we observed the formation of large TFAM (mitochondrial
171 transcription factor A)- and DNA-positive foci in the mitochondrial network in response to chronic Pb
172 treatment, indicative of aggregated mitochondrial nucleoids (Fig. 4A, B, C, D). This was greatest in
173 Δ*ATG5* cells, underscoring the relationship between sustained presence of damaged lysosomes and
174 the mitochondrial response to Pb. Corroborating the nucleoid imaging data, similar results were
175 obtained when aggregated nucleoids were alternately imaged by staining for FAST kinase domains 2
176 (FASTKD2), which marks nucleoid-associated RNA processing granules [56] (Fig. 4E, F). Further
177 consolidating the lysosomal association with the mitochondrial stress response, chronic treatment
178 with LLOMe also engendered nucleoid aggregation (Fig. 4G, H). Finally, robust mitochondrial nucleic
179 acid stress responses were also detected in wild-type MCF7 cells treated with Pb or LLOMe (Fig. 4I, J).
180 Taken together, the above data demonstrate that chronic lysosome damage is associated with
181 mitochondrial stress responses.

182

183 **Palbociclib treatment triggers mitochondrial nucleic acid release into the cytosol and interferon**
184 **responses**

185 Given the detection of mitochondrial nucleic acid stress upon Pb-mediated lysosome damage, we next
186 sought to directly detect immunostimulatory nucleic acid release from mitochondria. We prepared
187 mitochondrion-free cytosolic extracts (Fig. 5A) from cell clones deleted for Δ*ATG5* or rescued by
188 reintroduction of *GFP-ATG5* [57]; use of these paired lines diminished potential clonal variation that
189 might have obscured subtle mitochondrial nucleic acid fluctuations. Cytosolic mitochondrial DNA and
190 RNA were found to be elevated in the cytosol in response to chronic Pb; again, this was more
191 prominent in Δ*ATG5* cells where lysosome damage is more poorly resolved (Fig. 5B, C). Given that Pb
192 is known to induce interferon responses, we set out to interrogate whether lysosome damage played
193 a role (and potentially thus cytoplasmic accumulation of mitochondrial nucleic acids). Firstly, we first
194 established that chronic Pb triggers interferon signalling, analysing hallmarks such as phosphorylation
195 of STAT1 (signal transducer and activation of transcription 1) and transcriptional activation of type III
196 interferons, i.e., *IFNL1*, and interferon response genes (IRGs), i.e., *ISG15*, *IFIT1* and *CXCL10*. Pb indeed
197 induced phosphorylation of STAT1 (Figs. 6A, B, S2) and transcriptional activation (Fig. 6C) in A549 cells

198 over 48 h, most prominently in Δ*ATG5* cells, correlating with the persistent lysosome damage known
199 to occur here. Furthermore, phosphorylation of STAT1 was seen when testing lower doses of Pb akin
200 to steady-state plasma concentrations achieved during clinical treatment, although with greater
201 latency (one week) (Fig. 6D). Also corroborating the link with lysosome damage, chronic LLOMe
202 treatment also induced interferon responses over 48 h (Fig. 6E, F). Finally, wild-type MCF7 cells also
203 exhibited interferon responses to chronic treatment with either Pb or LLOMe (Fig. 6G, H, I, J). Taken
204 together, the above data indicate that chronic lysosome damage is a contributor to induction of
205 interferon responses.

206

207 **Mitochondrial nucleic acids are required for the interferon response to chronic lysosome damage**

208 To test whether the observed release of mitochondrial nucleic acid triggers the interferon signalling
209 associated with Pb-induced lysosome damage, we next depleted mitochondrial genomes from A549
210 control (Rescue) and Δ*ATG5* cells, via chronic dideoxy-cytidine treatment, generating "Rho0" cultures
211 (Fig. S3A). Importantly, mitochondrial nucleic acid depletion inhibited engagement of downstream
212 markers of interferon production by Pb, including phosphorylation of STAT1 (Fig. 7A, B), and
213 transcriptional upregulation of *IFNL1* and *ISG15* (Fig. 7C). Two modes of nucleic acid efflux from
214 mitochondria have been postulated in the prior literature. The first is associated with stereotypical
215 markers of mitochondrial nucleic acid stress, as observed in Fig. 3, and can be blocked using the VDAC
216 channel inhibitor VBIT-4 [53-55]. The second is characterised by a requirement for mitochondrial BAK
217 (BCL2 antagonist/killer 1) and BAX (BCL2-associated X, apoptosis regulator) pore-forming proteins [58,59].
218 We found that interferon responses to Pb were indeed abrogated by VBIT-4 treatment (Fig. 7D, E) but
219 not *BAK* and *BAX* double knockout (Fig. S3B). This observation further corroborates the link between
220 the mitochondrial nucleic acid stress induced by lysosome damage and interferon signalling. In line
221 with this, chronic LLOMe treatment was also unable provoke phosphorylation of STAT1 in Rho0 cells
222 (Fig. 7F, G). Finally, given the association of mitochondrial depolarisation with at least some forms of
223 mitochondrial perturbation, we assessed this; however, Δ*ATG5* cells did not show depolarisation as
224 assessed by flow cytometry with JC-10 dye, whereas they did respond in this manner to a positive
225 control drug, GTTP (Gamitrinib-triphenylphosphonium) [60] (Fig. 7H). Taken together with our prior
226 findings, the above data demonstrate that lysosome damage triggers accumulation of mitochondrial
227 nucleic acid in the cytosol, and that this drives interferon responses. However, Pb also reportedly
228 triggers interferon responses by suppressing CDK4/6-mediated silencing of nuclear genome-derived
229 dsRNA [34]. Given that we observe that CDK4/6-independent lysosome damage is associated with
230 mitochondrial nucleic acid release, we hypothesised co-operation between on-target (kinase activity)

231 and off-target (lysosomal-mitochondrial) effects of Pb. Indeed, *CDK4/6* deletion, while insufficient to
232 engage robust interferon responses alone, synergised with Pb treatment to induce a maximal
233 response (Fig. 7I, J). Taking the above data together, we conclude that sustained suppression of
234 CDK4/6 kinase activity has the potential to engage interferon signalling via non-mitochondrial routes
235 [34], but that the lysosome-mitochondrion axis must co-operate to fully realise the interferon effect, at
236 least in the context of Pb treatment.

237

238

Discussion

239 Our findings support the following model (Fig. 8). In response to chronic exposure to the
240 lysosomotropic cancer therapeutic Palbociclib (Pb), persistent lysosome rupture is invoked. Acute
241 lysosome damage typically leads to repair, removal and/or replacement of the damaged organelle.
242 These responses are at the core of the ELDR. We propose that in cells where chronic lysosome damage
243 is insufficient to trigger cell death, propagation of stress signalling via lysosome-mitochondrion
244 association leads to accumulation of cytosolic, self-derived immunostimulatory nucleic acids,
245 triggering interferon signalling. Indeed, other recent data have hinted that stress signals emanating
246 from acutely damaged lysosomes trigger wider changes in cell physiology [30-32]. However, we
247 acknowledge that – despite the triggering of such mitochondrial phenomena also by the tool
248 compound LLOMe – it is possible that direct effects of Palbociclib on mitochondria contribute to this
249 phenotype.. It is also possible the involvement of other organelles that form contacts with both
250 mitochondria and lysosomes – such as the endoplasmic reticulum (ER) [61] – could be involved in
251 lysosome-mitochondrial communication, but this remains to be tested.

252

253 In the case of Pb treatment, the mitochondrial response associated with lysosome damage is required
254 for interferon signalling but maximal stimulation occurs in co-operation with the known CDK4/6-
255 inhibitory activity of the drug, explaining fully this important anti-cancer facet of Pb action.
256 Instructively, mitochondrial nucleic acids may similarly be required to license interferon responses
257 after *Salmonella* infection [62]. This is suggestive when one considers that bacterial phagosome damage
258 by infectious agents can also engage selective autophagy mechanisms with molecular parallels to
259 lysophagy [2]. Furthermore, it has been recently suggested that damage to lysosomes invoked by
260 pathogens effects broad changes in mitochondrial proteome, secondarily to vesicular rupture [63].
261 Taking these observations together, we speculate that mitochondrial responses associated with
262 lysosome damage may have initially evolved to consolidate infection responses by priming interferon

263 responses, but not in itself triggering maximal signalling, i.e., co-operating with additional stimuli such
264 as nucleic acids or other patterns physically derived from the infectious agent. However, these ideas
265 require future exploration.

266

267 Our data show that the lysosome damage-induced interferon response depends on chronic
268 perturbation. For instance, A549 cells deleted for Δ*ATG5*, which are deficient in the ELDR, show a more
269 robust response to Pb and LLOMe, which correlates with more sustained lysosome damage. Similarly,
270 wild-type MCF7 cells show evidence of resolution of lysosome damage but more slowly than wild-type
271 A549 cells, and this again correlates with a more readily detectable interferon response. However, it
272 is possible that other functions of *ATG5* in autophagy pathways, for instance degradation of PRRs,
273 could also contribute to the observed *ATG5*-dependency in A549 cells [64-67]. Similarly, the loss of
274 mitophagy in these *ATG5*-deficient cells could also contribute to high levels of interferon response [68].
275 Overall, our data nonetheless still establish an association between lysosome damage and
276 engagement of interferon responses via mitochondrial release of nucleic acid.

277

278 Finally, our results highlight an important consideration when investigating small-molecule
279 therapeutics for cancer. The lysosome is sometimes considered a passive problem for therapy, in that
280 it sequesters basophilic drugs from their site of action [33]. Although the mitochondrion is implicated
281 here in response to Pb, it is unlikely that it will ultimately prove to be the only consequential signalling
282 hub responding to chronic lysosome damage. Indeed, we would suggest that off-target signalling
283 effects of cancer therapeutic drugs consequent from chronic accumulation in the lysosome should be
284 factored into cell-based drug action studies in future. This will facilitate holistic understanding of
285 therapeutic compound action and thus, ultimately, promote refinement of clinical applications.

286 ## Acknowledgements

287 We thank Richard Youle, Viktor Korolchuk, Noor Gammoh, Felix Randow for reagents. We thank Noor
288 Gammoh and Alex von Kriegsheim for feedback. We thank Steven Mitchell for assistance with electron
289 microscopy. For the purpose of open access, the author has applied a CC-BY public copyright licence
290 to any Author Accepted Manuscript version arising from this submission.

291 ## Funding

292 This work was supported by a Cancer Research UK (C20685/A29576 to S.W.).

293

294

295 ## Methods

296 **Cell culture and cell lines**

297 Cells were cultured in DMEM supplemented with 10% FBS, 2 mM L-glutamine and 10 U ml^{-1} 10 μg ml^{-}
298 ^{1} penicillin/streptomycin, at 37°C under 5% CO_2. At monthly intervals all cells in culture were tested
299 for the presence of mycoplasma. A549 NT, Δ*ATG5* and Rescue (Δ*ATG5* + GFP-ATG5) lines were
300 described previously by the authors and are a derivative of the A549:EcoR parental cell line, which is
301 A549 human lung adenocarcinoma cells derivatised to express Ecotropic receptor to enable
302 transduction with retrovirus with murine tropism [69]. MCF7:EcoR cells were newly generated, by the
303 same protocol, in this study, from parental MCF7 cells. Parental A549:EcoR and MCF7 breast
304 carcinoma lines were from the authors' laboratory and were verified by microsatellite genotyping.
305 YFP-GAL8 expressing retrovirus (see **Plasmids**) was used to generate stable A549 line pool, as
306 described previously [69]; pools of transductants were selected with 10 μg ml^{-1} blasticidin for 10 days.
307 Stable MCF7 cell pools expressing YFP-GAL8 were similarly generated from parental MCF7-EcoR cells
308 (selection in 50 μg ml^{-1} blasticidin). A549-EcoR cells stably expressing mRFP-GFP-GAL8 were made by
309 lentivirus transduction (see **Plasmids**) and a pool of transductants selected with 10 μg ml^{-1} blasticidin.
310 A549-EcoR and MCF7 cells stably expressing SRAI-GAL8 were created by lentiviral transduction (see
311 **Plasmids**) and selection with 10 μg ml^{-1} blasticidin. Then, cell populations expressing high YPet and
312 TOLLES fluorescent levels were enriched using a FACSAria II (BD Bioscience, San Jose, CA). To enable
313 both pooled and single clone CRISPR/Cas9 knockouts in A549-EcoR cell lines, stable expression of Cas9
314 was achieved by transducing lentivirus made from LentiCas9-Blast template and selection with 10 μg
315 ml^{-1} blasticidin. CRISPR/Cas9-mediated knockout in the resulting lines expressing Cas9 was performed
316 using lentiviral delivery of gRNA. Non-targeting/targeting sgRNA was cloned into lentiGuide-puro for
317 lentivirus production, and transductants selected for with 2.5 μg ml^{-1} puromycin. gRNA sequences
318 were: GFP (NT): GTGAACCGCATCGAGCTGAA; Luciferase (NT-2): AACGGCGGCGGGAAGTTCAC; MAVS:
319 TCTTCAATACCCTTCAGCGG; CDK4: TGTAGTGATGCGCGACGACA; CDK6: CTATTACTGAGCTCGATGTG;
320 BAX: GGCGGTGATGGACGGGTCCG; BAK: GGAACTCTGAGTCATAGCGT. Where single cell clones were
321 used, this was achieved via limiting dilution. All lentivirus was packaged in HEK293T cells according to
322 standard protocols; briefly, viral vector was co-transfected with pMD2.G and psPAX2 packaging
323 plasmids using Lipofectamine 2000.

324

325 **Drug treatments**

326 Seeding density was normalised per experiment treatment requirements. Cells were plated to be
327 approaching confluency, but not yet confluent, at the point of analysis. Typically, one third of the
328 number of cells to be treated with higher doses (e.g. 10 μM) Pb (Pb-HCL, Cayman #16273, dissolved
329 in DMSO) were seeded relative to the cognate DMSO vehicle treatments for 48 h treatments, and one
330 half for 24 h treatments, to compensate the cytostatic effect of Pb. For 10 μM Pb treatment, treatment
331 was applied once for the entire duration. For longer term treatments using 500 nM Pb, cells were
332 plated on day 0, treatment was initiated on day 1, and medium was refreshed with new drug or vehicle
333 at day 4. LLOMe (LLOMe-HCL, Cayman #16008, dissolved in DMSO) was dosed at 700 μM. VBIT-4
334 (Selleckchem #S3544) was dissolved in DMSO and used at 10 μM.

335

336 **Mitochondrial genome depleted cultures**

337 To generate paired Rho^{+} and Rho0 cultures, cells were cultured in standard medium supplemented
338 with 200 μM uridine (Sigma #U3750) and, for Rho0 culture, with an additional 10 μM ddC (2',3'-
339 dideoxycytidine, Sigma #D5782) for 14 consecutive days [48]. Cells were then maintained in culture for
340 a maximum of another week in medium still supplemented with ddC.

341

342 **Plasmids**

343 See Table S1 for full list. Where Gateway cloning was performed this was as per standard protocols
344 using BP clonase II and LR clonase II (Invitrogen). sgRNA cloning into lentiGuide-puro vector was
345 performed using restriction digestion as per the standard protocols available from Addgene. Detailed
346 sequence maps are available from authors upon request.

347

348 **Immunoblotting**

349 Cells were lysed in 4% SDS lysis buffer (4% SDS, 50 mM Tris-HCl pH 7.5 and 150 mM NaCl), followed
350 by pulse sonication. Protein concentration was measured by BCA protein assay, using the Pierce™ BCA
351 protein assay kit (Thermo Fisher, #23225). Normalised protein samples were diluted in Laemmli buffer
352 (4% SDS, 20% glycerol, 10% 2-mercaptoethanol, 0.125 M Tris-HCl pH 6.8, bromophenol blue) and
353 briefly heated to 95°C. SDS-PAGE was carried out using either 4-12% NuPage™ Bis-Tris Precast mini,
354 or 4-12% Novex™ Tris-Glycine precast midi gels (Thermo Fisher), in 1x NuPage™ MOPS SDS running
355 buffer (Thermo Fisher) or Pierce™ Tris-Glycine SDS running buffer (Thermo Fisher), respectively. Wet
356 transfer was used to transfer protein from mini gels, performed onto 0.2 μm nitrocellulose membrane

357 (GE Life Sciences), and semi-wet transfer system (Trans-blot turbo, Bio-Rad) was used to transfer
358 proteins from midi gels. Membranes were blocked in 5% BSA (Sigma) in PBS for 1 h at room
359 temperature (RT). All washes were performed three times in TBS - 0.1% Tween 20 (TBST), for 10 min
360 each at RT. Primary antibody dilution was in 0.1% BSA in PBS with 0.05% sodium azide, typically at
361 1:1000 except for α-Tubulin (1:50000). Membranes were incubated in primary antibody solution
362 overnight at 4 °C. The following antibodies were used: anti-ATG5 (Sigma, #A0731), anti-Calnexin (Cell
363 Signalling Technology [CST], #2679), anti-CDK4 (CST, #12790), anti-CDK6 (CST, #3136), anti-ISG15 (CST,
364 #2743), anti-MAVS (CST, #3993), anti-phosho-Y701-STAT1 (CST, #9167), anti-STAT1 (CST #9176), anti-
365 TOM20 (Santa Cruz, #sc-17764), anti-Cytochrome C apoptosis antibody cocktail (Abcam, #ab110415)
366 and anti-α-Tubulin (Sigma, #T9026). Secondary antibody solution was 0.1% powdered milk in TBST in
367 1:3000 dilution. Membranes were incubated with cognate HRP-linked secondary antibody (CST) for 1
368 h at RT. For detection, membranes were incubated in ECL reagent (ECL prime, Western blotting
369 reagent, GE Life Sciences) for 5 min at RT, or ECL reagent (1 M Tris-HCl pH 8.5, 250 mM luminol, 90
370 mM coumaric acid and 0.002% H_2O_2) for 1 min at RT, followed by film exposure and development
371 (AGFA automated developer), or chemiluminescent imaging (Amersham ImageQuant 800, software
372 v1.2.0). Relative protein band intensities were quantified using FIJI (v2.1.0). For P-STAT1, this is given
373 as a ratio to tubulin, as STAT1 itself is an interferon stimulated gene. Uncropped blots are shown in
374 Figs. S4-6.

375

376 **Immunostaining**

377 For immunofluorescence experiments, cells were typically seeded onto round 16 mm cover glass
378 (Fisher Scientific) except for super-resolution microscopy where cells were seeded on high-precision
379 cover glass (Zeiss™, Fisher Scientific). Cells were fixed in 4% paraformaldehyde (PFA) / PBS for 10 min
380 at RT and washed once in PBS. Permeabilization was performed for 10 min at RT using 0.25% Triton X-
381 100 (Sigma) / PBS, followed by another PBS wash. Primary and secondary antibody solution was
382 diluted in PBS / 1% BSA, typically at 1:200 (except p62 used at 1:1000). Secondary antibody solution
383 typically contained DAPI at 1:2500. Cells were incubated with primary antibody solution for 1 h, at RT,
384 followed by 3 x 5 min PBS washes. The following antibodies were used: anti-DNA (EMD Milipore,
385 #CBL186), anti-FASTKD2 (Proteintech, #17464-1-AP), anti-LAMP2 (Abcam, #ab25631), anti-TFAM (CST,
386 #8076), anti-TOM20 (CST, #42406) (used when co-staining with mouse antibodies), anti-TOM20 (Santa
387 Cruz, #sc-17764) (used when co-staining with rabbit antibodies and YFP-GAL8) and anti-DNA (Merck-
388 Millipore, #CBL186). Secondary antibody was cognate fluorophore linked secondary antibody (Thermo
389 Fisher, Alexa Fluor). Secondary antibody solution was applied to cells for 45 min, at RT, followed by 3

390 x 5 min PBS washes. Regular cover glass was mounted onto a microscope slide using DAKO
391 fluorescence mounting medium. High-precision cover glass super-resolution microscopy was
392 mounted using Fluoromount™ aqueous mounting medium (Sigma).

393

394 **Fluorescence Microscopy**

395 For widefield immunofluorescence microscopy, images were taken with Olympus BX51 fluorescent
396 microscope (Cell^F software). For confocal microscopy, images were taken using a Nikon A1R laser-
397 scanning confocal microscope. Images are presented as maximum projection Z-stacks. Super-
398 resolution images were acquired using Super Resolution Optical Photon Reassignment Microscopy on
399 a Nikon Eclipse Ti2 inverted microscope stand and a SR Apo TIRF 100x 1.49NA oil lens (Nikon
400 Instruments). The CMOS cameras used for acquisition were Teledyne Photometrics Prime 95B
401 (Teledyne Photometrics 3440 E.Britannia Drive, Tucson AZ) and 405, 488, 561, 640nm laser lines.
402 Acquisition of images and deconvolution was carried out using Nikon NIS-Elements Advanced
403 Research software (v5.21-03). For imaging SRAI-GAL8, cells were plated on glass bottom 96 well plates
404 (P96-1.5H-N, Cellvis) at 70-90% confluency. Cells were fixed with 4% paraformaldehyde in PBS, pH 7.2
405 at room temperature for 10 mins. Cells were then washed twice with PBS and kept at 4°C. Cells were
406 imaged 1-3 days after fixation while immersed in PBS. Images were captured with a Nikon Eclipse Ti-
407 E inverted microscope (Nikon Instruments UK Ltd, Kingston Upon Thames, UK) using a 40X objective.
408 Widefield illumination for this was provided by a CoolLED PE-4000 LED light source (CoolLED Ltd,
409 Andover, UK) combined with LED-CFP/YFP/mCherry-3X-A (Pinkel) filter sets (IDEX Health & Science,
410 LLC, Center of Excellence, 1180 John Street, Rochester, New York 14586, United States). Images were
411 acquired with a Photometrics Prime BSI sCMOS camera (Teledyne Photometrics, 3440 E. Britannia
412 Drive, Suite 100, Tucson, AZ 85706). Conditional imaging was setup and controlled using the Nikon
413 Nis-Elements JOBS module. The JOB (script) incorporates automated two wavelength capture of 3D
414 images (Z stacks for CFP and YFP filters) from an array of imaging sites (XY positions) using a motorised
415 XY stage within user selected wells (a total of 7 fields per well were imaged). SRAI-GAL8 images are
416 shown as z-projections from 5 z-steps.

417

418 **SRRF Time-lapse videomicroscopy**

419 Time-lapse videomicroscopy was performed by exchanging full medium for phenol-red free medium
420 containing 0.132 μg ml^{-1} MitoTracker Red and fresh Pb 30 mins prior to imaging. Images were acquired
421 on the multimodal Imaging Platform Dragonfly (Andor technologies, Belfast UK) equipped with 405,

422 445, 488, 514, 561, 640 and 680nm lasers built on a Nikon Eclipse Ti-E inverted microscope body with
423 Perfect focus system (Nikon Instruments, Japan). Super Resolution Radial Fluctuations (SRRF) data
424 were acquired using the iXon 888 EMCCD camera and a 100x SR Apo TIRF 1.49NA objective lens.
425 Environmental control of the cultured cells was maintained during imaging with an Okolab bold line
426 stage top incubation chamber incorporating temperature and humidified CO2 control (Okolab S.R.L,
427 Ottaviano, NA, Italy).

428

429 **Transmission electron microscopy (TEM)**

430 Fixative solution was prepared by mixing fresh aqueous 16% paraformaldehyde (from methanol-free
431 powder, Sigma) and fresh 25% EM grade glutaraldehyde (Merck) to final concentration 2%
432 paraformaldehyde, 2.5% glutaraldehyde in 0.1 M PHEM buffer (120 mM PIPES, 50 mM HEPES, 4 mM
433 $MgCl_2$ and 20 mM EGTA, pH 6.9). Two 15 cm dishes per condition of cells were used and cells pelleted
434 by centrifugation 200 g for 3 min in a 15 mL tube. Cells were resuspended in the fixative solution and
435 incubated for 20 min at room temperature, on a slow-motion roller bank. Cells were then centrifuged,
436 supernatant removed, and fresh fixative solution added. The second fixative solution was incubated
437 with cells for 4 h at room temperature, on a slow-motion roller bank. The cells were washed 3 times
438 with 0.1 M PHEM buffer and stored in 0.1 M PHEM until embedding in EPON resin at 4°C (2-3 days).
439 Sections were co-stained with uranyl acetate and lead citrate to provide membrane contrast. TEM
440 images were taken by JEOL JEM-1400 series, 120 kV transmission electron microscope.

441

442 **Image analyses**

443 From SRAI-GAL8 images, a TOLLES:YPet index was obtained using an ImageJ macro that calculates the
444 percent area of pixels with TOLLES:YPet ratio above a given ratio over the total area that the
445 fluorophore occupies within the field [50]. A ratio of 1.75 was used. Substructures in cells (foci,
446 lysosomes, nuclei) were generally counted manually using ImageJ cell counter plug-in. In the specific
447 instance of TFAM nucleoid aggregates, these were counted using the ImageJ Particle Analysis tool
448 (automated particle count with a minimum detected particle area threshold of 0.7 μm^2. Parameters
449 from TEM images (cytosol area, lysosome area, mitochondria-lysosome contact length) were
450 measured using the ImageJ ROI manager. The number of galectolysosomes formed in mRFP-GFP-
451 Galectin-8 cells were determined by counting GFP quenched, mRFP positive foci using the ImageJ
452 MitoQC plug-in [70].

453

454 Images obtained by SoRa were 3D deconvoluted using NIS elements imaging software (Nikon, v5.21-
455 03) and further analysed using Imaris software (v9.9.1). YFP-GAL8 foci were modelled as centroids.
456 Similarly, the mitochondria network surface masking was applied according to the intensity of TOM20
457 fluorescent signal. The same modelling settings were used on all images acquired. Standard Imaris
458 measurements were extracted showing the distance from the YFP-GAL8 foci to the rendered
459 mitochondrial network, measured from the centre of modelled YFP-GAL8 centroids to the outer
460 surface of the modelled mitochondrial network, with the radius of the centroid then subtracted. To
461 assess association of YFP-GAL8 foci with the mitochondrial network, they were compared with a
462 shuffled control. In these controls, an ImageJ plug-in was created to randomly shuffle the YFP-GAL8
463 foci within the cytosolic area on a per cell basis (cytosolic area as outlined by the reach of the
464 mitochondrial network).

465

466 **Cytosol fractionation for nucleic acid quantification**

467 Methods were adapted from previously published protocols [47,71]. Cells were trypsinised and fresh
468 medium added to inactivate trypsin, then centrifuged at 200 g at 4 °C. The supernatant was then
469 aspirated, and cells washed by gentle pipetting in 1 ml of ice-cold PBS. The centrifugation and PBS
470 wash was repeated once more. The pellet was then resuspended in 500 µl (per 60 mm dish) of ice-
471 cold fractionation buffer (50 mM HEPES pH 7.4, 150 mM NaCl, 25 µg ml^{-1} fresh digitonin (Sigma,
472 #11024-24-1) and 1 X Complete Protease Inhibitor Cocktail with EDTA, Roche). When RNA was to be
473 isolated from the cytosolic fractions 4 U RNase inhibitor (Promega, #N2111) was added to the
474 fractionation buffer. The suspensions were incubated end-over-end for 10 mins at 4 °C to allow
475 selective plasma membrane permeabilization, then centrifuged at 1000 g for 3 min to pellet cells
476 (insoluble fraction). The cytosolic supernatant was transferred to a fresh tube, pelleted at 1000 g for
477 3 mins, and the resulting cleared supernatant transferred to a fresh tube. This cytosolic supernatant
478 was finally centrifuged at 17000 g for 10 min to pellet any remaining non-cytosolic cellular material or
479 debris. The cytosolic fraction was transferred to a fresh tube. The insoluble fraction was solubilised in
480 in 4% SDS lysis buffer (4% SDS, 50 mM Tris-HCl pH 7.5 and 150 mM NaCl), 300 µL of lysis buffer per 60
481 mm dish, and pulse sonicated.

482

483 In those instances where the cytosolic fraction was to be used for DNA abundance quantification, an
484 additional step was introduced into the above procedure where, after initial cell trypsinisation, one-
485 third of the cell suspension was separately pelleted and lysed by addition of 400 µl of 50 µM NaOH,

486 followed by heating at 95°C for 30 min to solubilise DNA, and neutralised by adding 50 µl 1 M Tris-HCL
487 (pH 8.0). These extracts served as normalisation controls (*ACTB* qPCR, see below)

488

489 **Nucleic acid purification**

490 For total cell RNA isolation, cells were lysed directly in RLT lysis buffer with added β-mercaptoethanol
491 as per manufacturer's protocol (Qiagen, RNeasy kit), and RNA was isolated using by spin-column RNA
492 extraction kit (Qiagen, RNeasy kit). For RNA isolation from cytosolic fractions (above), Trizol /
493 chloroform extraction was performed. Briefly, cytosolic fractions were mixed with Trizol (Thermo
494 Fisher, #15596026) in a 1:1 ratio and incubated for 5 min. 0.2 mL of chloroform per 1 mL of Trizol was
495 added to the mixture and vortexed vigorously for 15 seconds, followed by incubation at room
496 temperature for 2 min. The mixture was centrifuged at 12,000 g for 15 min at 4°C. Following
497 centrifugation, the upper aqueous phase was transferred carefully into a fresh RNase-free tube. 25 µg
498 of GlycoBlue coprecipitant (Thermo Fisher, #AM9516) was added and RNA precipitated by mixing with
499 0.5 mL of isopropanol per 1 ml of original Trizol reagent used, then incubation at room temperature
500 for 10 min, followed by centrifugation at 12,000 g for 10 min at 4°C. The supernatant was removed
501 completely and discarded. The RNA pellet was washed once with 1 ml of 75% ethanol per 1 ml of
502 original Trizol reagent used, and subsequent centrifugation at 7,500g for 5 min at 4°C. The ethanol
503 wash was then fully removed, and the cleaned RNA pellet air-dried for 10 min, then re-dissolved in
504 nuclease free water. To remove trace DNA, samples were treated with DNase-I using the RNAqueous
505 DNase kit (Thermo Fisher), according to the manufacturer's protocol. For DNA isolation from cytosolic
506 fractions (above), a spin-column DNA isolation kit (QIAamp, Qiagen) was used, according to the
507 manufacturer's protocol. DNA was eluted in nuclease-free water. Nucleic acid concentration and
508 purity was measured using a NanoDrop 2000c spectrophotometer (Thermo Scientific).

509

510 **Quantitative PCR (qPCR)**

511 Reverse transcription from RNA isolated from total cell lysates was done using QScript cDNA SuperMix
512 (QuantaBio #95048), according to the manufacturer's protocol. Reverse transcription from RNA
513 isolated from cytosolic fractions (above) was performed using the SuperScript III reverse transcriptase
514 (Thermo Fisher, cat.no 18080093). In both instances, random DNA hexamers were used for priming.
515 qPCR was performed using SYBR Select Master Mix (Applied Biosystems, #4472908), according to the
516 manufacturer's protocol, on a StepOne Real-Time PCR System instrument (ThermoFisher). For cDNA
517 from total cell RNA samples, transcripts were quantified using the ΔΔCt method, while standard curve

518 methodology was used to quantify cDNA/DNA obtained from cytosolic fractions. Each independent
519 replicate data point is typically the mean of 3 technical replicates. Primers used are listed in Table S2.

520

521 **Flow cytometry**

522 Δ*ATG5* A549 cells were plated in 6-well plates. The following day, cells were treated with DMSO or 10
523 µM Pb for 24 h. 4h 20 µM Gamitrinib TPP (GTPP, MedChemExpress, HY-102007A) treatment was
524 performed on the following day prior to incubation with JC-10. After corresponding times, cells were
525 incubated with 15 µM JC-10 (Enzo, #ENZ-52305) or 50 nM LysoTracker™ Red DND-99 (Invitrogen,
526 #L7528) in non-phenol red DMEM media (Gibco, #31053028) (supplemented with 10% FBS, 2 mM L-
527 glutamine and 10 U ml^{-1} 10 µg ml^{-1} penicillin/streptomycin) for 30 min at 37°C. Cells were then washed
528 with PBS, trypsinised for 5 min and fresh flow cytometry buffer (non-phenol red DMEM media
529 supplemented with 1% FBS, 2 mM L-glutamine and 10 U ml^{-1} 10 µg ml^{-1} penicillin/streptomycin) was
530 added to stop the reaction. Cells were centrifuged at 150 g for 3 min, resuspended in 500 µl of flow
531 cytometry buffer and kept on ice until analysed in a Cytoflex S flow cytometer (Beckman Coulter). JC-
532 10 monomeric was excited by a 488 nm laser line and emission collected through a 525/40BP. JC-
533 aggregates were excited with a 561 nm laser line and emission was collected through 585/42BP. To
534 quantify the changes in mitochondrial membrane potential the fluorescent ratio of
535 aggregating/monomeric JC-10 was used. Lysotracker red was excited by a 561 nm laser line and its
536 emission was collected through 610/20BP. Data was exported and analysed using FlowJo v10.10
537 software.

538

539 **Statistical analyses**

540 All statistical analysis was carried out using GraphPad (Prism) (version 9.5.1). Sample size for
541 experiments to provide adequate power were predicted based upon prior experience of the
542 experimenter and/or pilot data sampling. All independent biological replicates are represented with
543 standard error of the mean (s.e.m.). In the case of electron microscopy image analyses, individual cells
544 are represented as data points and variance described as standard deviation (s.d.). Tests are detailed
545 in figure legends. In general, an assumption of normality was made and all tests were two-sided. Thus,
546 where pairwise comparisons between two samples are performed, this is performed with an unpaired
547 Student's t-test or a one-sample t-test (latter instance when comparing against the normalisation
548 control). In a minority of cases where a non-normal distribution was clearly observed, a one-sample
549 Wilcoxon test was instead used for pairwise comparison (as indicated in figure legends). When

multiple comparisons were performed in instances where there was only one independent variable, we generally used one-way ANOVA with Holm-Šídák testing. Where multiple comparisons were performed in instances of two independent variables in data set (e.g., cell line identity and/or drug application) we generally performed two-way ANOVA with Holm-Šídák testing. In the case of cytosolic RNA/DNA analysis, ratio paired t-tests were performed. Replicates containing outliers as detected by the Grubb's test were removed prior to the ratio paired t-test. Comparison of pairs of frequency distributions were performed by the Kolmogorov-Smirnov test for each of three replicates, and a *P*-value for each replicate generated individually.

Code availability

The custom FIJI (ImageJ) plug-in macro to shuffle galectin-8 foci within cell space is reproduced below:

```
1. # get current image, a image with labelled objects
2. plus=WindowManager.getCurrentImage()
3. # wrap ImagePlus into 3D suite image format
4. img=ImageInt.wrap(plus)
5. # create a population of 3D objects
6. pop=Objects3DPopulation(img)
7. # create a mask where to shuffle objects
8. # here same as input image
9. IJ.selectWindow("mask");
10. plus2=WindowManager.getCurrentImage()
11. maskimg=ImageInt.wrap(plus2)
12. obj=Object3Dvoxels(maskimg)
13. pop.setMask(obj)
14. # get the shuffled objects and build a population from them
15. listObjects=pop.shuffle()
16. pop2=Objects3Dpopulation(listObjects)
17. # draw the results
18. res = ImageShort("res", img.sizeX, img.sizeY, img.sizeZ)
```

```
19. pop2.draw(res)
20. res.show("shuffle")
```

Data Availability

All relevant data and details of resources can be found within the article and its supplementary information. Uncropped blots are shown in Figs. S4-6. Raw data not included in this manuscript are available from the corresponding author upon reasonable request. Plasmids, cell lines and other reagents are available from the corresponding author upon reasonable request.

Additional Information

The author(s) declare no competing interests.

591 ## References

592 1 Zoncu, R. & Perera, R. M. Built to last: lysosome remodeling and repair in health and disease.
593 *Trends Cell Biol* **32**, 597–610, doi:10.1016/j.tcb.2021.12.009 (2022).
594 2 Thurston, T. L., Wandel, M. P., von Muhlinen, N., Foeglein, A. & Randow, F. Galectin 8 targets
595 damaged vesicles for autophagy to defend cells against bacterial invasion. *Nature* **482**, 414–
596 418, doi:10.1038/nature10744 (2012).
597 3 Wang, F., Gomez-Sintes, R. & Boya, P. Lysosomal membrane permeabilization and cell death.
598 *Traffic* **19**, 918–931, doi:10.1111/tra.12613 (2018).
599 4 Radulovic, M. *et al.* ESCRT-mediated lysosome repair precedes lysophagy and promotes cell
600 survival. *EMBO J* **37**, e99753, doi:10.15252/embj.201899753 (2018).
601 5 Skowyra, M. L., Schlesinger, P. H., Naismith, T. V. & Hanson, P. I. Triggered recruitment of
602 ESCRT machinery promotes endolysosomal repair. *Science* **360**, doi:10.1126/science.aar5078
603 (2018).
604 6 Tan, J. X. & Finkel, T. A phosphoinositide signalling pathway mediates rapid lysosomal repair.
605 *Nature* **609**, 815–821, doi:10.1038/s41586-022-05164-4 (2022).
606 7 Jia, J. *et al.* Galectin-3 Coordinates a Cellular System for Lysosomal Repair and Removal. *Dev*
607 *Cell* **52**, 69–87 e68, doi:10.1016/j.devcel.2019.10.025 (2020).
608 8 Papadopoulos, C., Kravic, B. & Meyer, H. Repair or Lysophagy: Dealing with Damaged
609 Lysosomes. *J Mol Biol* **432**, 231–239, doi:10.1016/j.jmb.2019.08.010 (2020).
610 9 Maejima, I. *et al.* Autophagy sequesters damaged lysosomes to control lysosomal biogenesis
611 and kidney injury. *EMBO J* **32**, 2336–2347, doi:10.1038/emboj.2013.171 (2013).
612 10 Dikic, I. & Elazar, Z. Mechanism and medical implications of mammalian autophagy. *Nat Rev*
613 *Mol Cell Biol* **19**, 349–364, doi:10.1038/s41580-018-0003-4 (2018).
614 11 Vargas, J. N. S., Hamasaki, M., Kawabata, T., Youle, R. J. & Yoshimori, T. The mechanisms and
615 roles of selective autophagy in mammals. *Nat Rev Mol Cell Biol* **24**, 167–185,
616 doi:10.1038/s41580-022-00542-2 (2023).
617 12 Hoyer, M. J., Swarup, S. & Harper, J. W. Mechanisms Controlling Selective Elimination of
618 Damaged Lysosomes. *Curr Opin Physiol* **29**, 100590, doi:10.1016/j.cophys.2022.100590
619 (2022).
620 13 Jia, J. *et al.* Galectins Control mTOR in Response to Endomembrane Damage. *Mol Cell* **70**, 120–
621 135 e128, doi:10.1016/j.molcel.2018.03.009 (2018).
622 14 Gahlot, P. *et al.* Lysosomal damage sensing and lysophagy initiation by SPG20-ITCH. *Mol Cell*
623 **84**, 1556–1569 e1510, doi:10.1016/j.molcel.2024.02.029 (2024).
624 15 Kravic, B. *et al.* Ubiquitin profiling of lysophagy identifies actin stabilizer CNN2 as a target of
625 VCP/p97 and uncovers a link to HSPB1. *Mol Cell* **82**, 2633–2649 e2637,
626 doi:10.1016/j.molcel.2022.06.012 (2022).
627 16 Papadopoulos, C. *et al.* VCP/p97 cooperates with YOD1, UBXD1 and PLAA to drive clearance
628 of ruptured lysosomes by autophagy. *EMBO J* **36**, 135–150, doi:10.15252/embj.201695148
629 (2017).
630 17 Eapen, V. V., Swarup, S., Hoyer, M. J., Paulo, J. A. & Harper, J. W. Quantitative proteomics
631 reveals the selectivity of ubiquitin-binding autophagy receptors in the turnover of damaged
632 lysosomes by lysophagy. *Elife* **10**, e72328, doi:10.7554/eLife.72328 (2021).
633 18 Gallagher, E. R. & Holzbaur, E. L. F. The selective autophagy adaptor p62/SQSTM1 forms phase
634 condensates regulated by HSP27 that facilitate the clearance of damaged lysosomes via
635 lysophagy. *Cell Rep* **42**, 112037, doi:10.1016/j.celrep.2023.112037 (2023).
636 19 Chauhan, S. *et al.* TRIMs and Galectins Globally Cooperate and TRIM16 and Galectin-3 Co-
637 direct Autophagy in Endomembrane Damage Homeostasis. *Dev Cell* **39**, 13–27,
638 doi:10.1016/j.devcel.2016.08.003 (2016).

20 Jia, J. *et al.* AMPK, a Regulator of Metabolism and Autophagy, Is Activated by Lysosomal Damage via a Novel Galectin-Directed Ubiquitin Signal Transduction System. *Mol Cell* **77**, 951–969 e959, doi:10.1016/j.molcel.2019.12.028 (2020).

21 Park, N. Y. *et al.* Activation of lysophagy by a TBK1-SCF(FBXO3)-TMEM192-TAX1BP1 axis in response to lysosomal damage. *Nat Commun* **16**, 1109, doi:10.1038/s41467-025-56294-y (2025).

22 Johansen, T. & Lamark, T. Selective Autophagy: ATG8 Family Proteins, LIR Motifs and Cargo Receptors. *J Mol Biol* **432**, 80–103, doi:10.1016/j.jmb.2019.07.016 (2020).

23 Lazarou, M. *et al.* The ubiquitin kinase PINK1 recruits autophagy receptors to induce mitophagy. *Nature* **524**, 309–314, doi:10.1038/nature14893 (2015).

24 Vargas, J. N. S. *et al.* Spatiotemporal Control of ULK1 Activation by NDP52 and TBK1 during Selective Autophagy. *Mol Cell* **74**, 347–362 e346, doi:10.1016/j.molcel.2019.02.010 (2019).

25 Turco, E. *et al.* FIP200 Claw Domain Binding to p62 Promotes Autophagosome Formation at Ubiquitin Condensates. *Mol Cell* **74**, 330–346 e311, doi:10.1016/j.molcel.2019.01.035 (2019).

26 Ravenhill, B. J. *et al.* The Cargo Receptor NDP52 Initiates Selective Autophagy by Recruiting the ULK Complex to Cytosol-Invading Bacteria. *Mol Cell* **74**, 320–329 e326, doi:10.1016/j.molcel.2019.01.041 (2019).

27 Bhattacharya, A. *et al.* A lysosome membrane regeneration pathway depends on TBC1D15 and autophagic lysosomal reformation proteins. *Nat Cell Biol* **25**, 685–698, doi:10.1038/s41556-023-01125-9 (2023).

28 Cross, J. *et al.* Lysosome damage triggers direct ATG8 conjugation and ATG2 engagement via non-canonical autophagy. *J Cell Biol* **222**, doi:10.1083/jcb.202303078 (2023).

29 Eriksson, I., Waster, P. & Ollinger, K. Restoration of lysosomal function after damage is accompanied by recycling of lysosomal membrane proteins. *Cell Death Dis* **11**, 370, doi:10.1038/s41419-020-2527-8 (2020).

30 Jia, J. *et al.* Stress granules and mTOR are regulated by membrane atg8ylation during lysosomal damage. *J Cell Biol* **221**, doi:10.1083/jcb.202207091 (2022).

31 Duran, J. *et al.* Calcium signaling from damaged lysosomes induces cytoprotective stress granules. *EMBO J* **43**, 6410–6443, doi:10.1038/s44318-024-00292-1 (2024).

32 Neuwirt, E. *et al.* Tyrosine kinase inhibitors can activate the NLRP3 inflammasome in myeloid cells through lysosomal damage and cell lysis. *Sci Signal* **16**, eabh1083, doi:10.1126/scisignal.abh1083 (2023).

33 Llanos, S. *et al.* Lysosomal trapping of palbociclib and its functional implications. *Oncogene* **38**, 3886–3902, doi:10.1038/s41388-019-0695-8 (2019).

34 Goel, S. *et al.* CDK4/6 inhibition triggers anti-tumour immunity. *Nature* **548**, 471–475, doi:10.1038/nature23465 (2017).

35 Fan, H. *et al.* DNA damage induced by CDK4 and CDK6 blockade triggers anti-tumor immune responses through cGAS-STING pathway. *Commun Biol* **6**, 1041, doi:10.1038/s42003-023-05412-x (2023).

36 Wu, J. *et al.* Separable Cell Cycle Arrest and Immune Response Elicited through Pharmacological CDK4/6 and MEK Inhibition in RASmut Disease Models. *Mol Cancer Ther* **23**, 1801–1814, doi:10.1158/1535-7163.MCT-24-0369 (2024).

37 Roulois, D. *et al.* DNA-Demethylating Agents Target Colorectal Cancer Cells by Inducing Viral Mimicry by Endogenous Transcripts. *Cell* **162**, 961–973, doi:10.1016/j.cell.2015.07.056 (2015).

38 Akira, S., Uematsu, S. & Takeuchi, O. Pathogen recognition and innate immunity. *Cell* **124**, 783–801, doi:10.1016/j.cell.2006.02.015 (2006).

39 Yoneyama, M. *et al.* The RNA helicase RIG-I has an essential function in double-stranded RNA-induced innate antiviral responses. *Nat Immunol* **5**, 730–737, doi:10.1038/ni1087 (2004).

40 Seth, R. B., Sun, L., Ea, C. K. & Chen, Z. J. Identification and characterization of MAVS, a mitochondrial antiviral signaling protein that activates NF-kappaB and IRF 3. *Cell* **122**, 669–682, doi:10.1016/j.cell.2005.08.012 (2005).

41 Rehwinkel, J. & Gack, M. U. RIG-I-like receptors: their regulation and roles in RNA sensing. *Nat Rev Immunol* **20**, 537–551, doi:10.1038/s41577-020-0288-3 (2020).

42 Sun, L., Wu, J., Du, F., Chen, X. & Chen, Z. J. Cyclic GMP-AMP synthase is a cytosolic DNA sensor that activates the type I interferon pathway. *Science* **339**, 786–791, doi:10.1126/science.1232458 (2013).

43 Crow, Y. J. & Stetson, D. B. The type I interferonopathies: 10 years on. *Nat Rev Immunol* **22**, 471–483, doi:10.1038/s41577-021-00633-9 (2022).

44 Zitvogel, L., Galluzzi, L., Kepp, O., Smyth, M. J. & Kroemer, G. Type I interferons in anticancer immunity. *Nat Rev Immunol* **15**, 405–414, doi:10.1038/nri3845 (2015).

45 Ishikawa, H. & Barber, G. N. STING is an endoplasmic reticulum adaptor that facilitates innate immune signalling. *Nature* **455**, 674–678, doi:10.1038/nature07317 (2008).

46 Mackenzie, K. J. *et al.* cGAS surveillance of micronuclei links genome instability to innate immunity. *Nature* **548**, 461–465, doi:10.1038/nature23449 (2017).

47 Dhir, A. *et al.* Mitochondrial double-stranded RNA triggers antiviral signalling in humans. *Nature* **560**, 238–242, doi:10.1038/s41586-018-0363-0 (2018).

48 Tigano, M., Vargas, D. C., Tremblay-Belzile, S., Fu, Y. & Sfeir, A. Nuclear sensing of breaks in mitochondrial DNA enhances immune surveillance. *Nature* **591**, 477–481, doi:10.1038/s41586-021-03269-w (2021).

49 Katayama, H. *et al.* Visualizing and Modulating Mitophagy for Therapeutic Studies of Neurodegeneration. *Cell* **181**, 1176–1187 e1116, doi:10.1016/j.cell.2020.04.025 (2020).

50 Jimenez-Moreno, N., Salomo-Coll, C., Murphy, L. C. & Wilkinson, S. Signal-Retaining Autophagy Indicator as a Quantitative Imaging Method for ER-Phagy. *Cells* **12**, doi:10.3390/cells12081134 (2023).

51 Wong, Y. C., Ysselstein, D. & Krainc, D. Mitochondria-lysosome contacts regulate mitochondrial fission via RAB7 GTP hydrolysis. *Nature* **554**, 382–386, doi:10.1038/nature25486 (2018).

52 Uzhachenko, R. V. *et al.* Metabolic modulation by CDK4/6 inhibitor promotes chemokine-mediated recruitment of T cells into mammary tumors. *Cell Rep* **35**, 109271, doi:10.1016/j.celrep.2021.109271 (2021).

53 West, A. P. *et al.* Mitochondrial DNA stress primes the antiviral innate immune response. *Nature* **520**, 553–557, doi:10.1038/nature14156 (2015).

54 Kim, J. *et al.* VDAC oligomers form mitochondrial pores to release mtDNA fragments and promote lupus-like disease. *Science* **366**, 1531–1536, doi:10.1126/science.aav4011 (2019).

55 Torres-Odio, S. *et al.* Loss of Mitochondrial Protease CLPP Activates Type I IFN Responses through the Mitochondrial DNA-cGAS-STING Signaling Axis. *J Immunol* **206**, 1890–1900, doi:10.4049/jimmunol.2001016 (2021).

56 Antonicka, H., Sasarman, F., Nishimura, T., Paupe, V. & Shoubridge, E. A. The mitochondrial RNA-binding protein GRSF1 localizes to RNA granules and is required for posttranscriptional mitochondrial gene expression. *Cell Metab* **17**, 386–398, doi:10.1016/j.cmet.2013.02.006 (2013).

57 Newman, A. C., Kemp, A. J., Drabsch, Y., Behrends, C. & Wilkinson, S. Autophagy acts through TRAF3 and RELB to regulate gene expression via antagonism of SMAD proteins. *Nat Commun* **8**, 1537, doi:10.1038/s41467-017-00859-z (2017).

58 Riley, J. S. *et al.* Mitochondrial inner membrane permeabilisation enables mtDNA release during apoptosis. *EMBO J* **37**, doi:10.15252/embj.201899238 (2018).

59 McArthur, K. *et al.* BAK/BAX macropores facilitate mitochondrial herniation and mtDNA efflux during apoptosis. *Science* **359**, doi:10.1126/science.aao6047 (2018).

60 Kang, B. H. *et al.* Combinatorial drug design targeting multiple cancer signaling networks controlled by mitochondrial Hsp90. *J Clin Invest* **119**, 454–464, doi:10.1172/JCI37613 (2009).

739 61 Voeltz, G. K., Sawyer, E. M., Hajnoczky, G. & Prinz, W. A. Making the connection: How
740 membrane contact sites have changed our view of organelle biology. *Cell* **187**, 257–270,
741 doi:10.1016/j.cell.2023.11.040 (2024).
742 62 Xu, L. *et al.* Salmonella Induces the cGAS-STING-Dependent Type I Interferon Response in
743 Murine Macrophages by Triggering mtDNA Release. *mBio* **13**, e0363221,
744 doi:10.1128/mbio.03632-21 (2022).
745 63 Bussi, C. *et al.* Lysosomal damage drives mitochondrial proteome remodelling and reprograms
746 macrophage immunometabolism. *Nat Commun* **13**, 7338, doi:10.1038/s41467-022-34632-8
747 (2022).
748 64 Nakahira, K. *et al.* Autophagy proteins regulate innate immune responses by inhibiting the
749 release of mitochondrial DNA mediated by the NALP3 inflammasome. *Nat Immunol* **12**, 222–
750 230, doi:10.1038/ni.1980 (2011).
751 65 Mathew, R. *et al.* Functional role of autophagy-mediated proteome remodeling in cell survival
752 signaling and innate immunity. *Mol Cell* **55**, 916–930, doi:10.1016/j.molcel.2014.07.019
753 (2014).
754 66 Prabakaran, T. *et al.* Attenuation of cGAS-STING signaling is mediated by a p62/SQSTM1-
755 dependent autophagy pathway activated by TBK1. *EMBO J* **37**, doi:10.15252/embj.201797858
756 (2018).
757 67 He, X. *et al.* RNF34 functions in immunity and selective mitophagy by targeting MAVS for
758 autophagic degradation. *EMBO J* **38**, e100978, doi:10.15252/embj.2018100978 (2019).
759 68 Jimenez-Loygorri, J. I. *et al.* Mitophagy curtails cytosolic mtDNA-dependent activation of
760 cGAS/STING inflammation during aging. *Nat Commun* **15**, 830, doi:10.1038/s41467-024-
761 45044-1 (2024).
762 69 Newman, A. C. *et al.* TBK1 kinase addiction in lung cancer cells is mediated via autophagy of
763 Tax1bp1/Ndp52 and non-canonical NF-kappaB signalling. *PLoS One* **7**, e50672,
764 doi:10.1371/journal.pone.0050672 (2012).
765 70 Montava-Garriga, L., Singh, F., Ball, G. & Ganley, I. G. Semi-automated quantitation of
766 mitophagy in cells and tissues. *Mech Ageing Dev* **185**, 111196,
767 doi:10.1016/j.mad.2019.111196 (2020).
768 71 Bryant, J. D., Lei, Y., VanPortfliet, J. J., Winters, A. D. & West, A. P. Assessing Mitochondrial
769 DNA Release into the Cytosol and Subsequent Activation of Innate Immune-related Pathways
770 in Mammalian Cells. *Curr Protoc* **2**, e372, doi:10.1002/cpz1.372 (2022).
771 72 Ran, F. A. *et al.* Genome engineering using the CRISPR-Cas9 system. *Nat Protoc* **8**, 2281–2308,
772 doi:10.1038/nprot.2013.143 (2013).
773 73 Yang, X. *et al.* A public genome-scale lentiviral expression library of human ORFs. *Nat Methods*
774 **8**, 659–661, doi:10.1038/nmeth.1638 (2011).
775 74 Campeau, E. *et al.* A versatile viral system for expression and depletion of proteins in
776 mammalian cells. *PLoS One* **4**, e6529, doi:10.1371/journal.pone.0006529 (2009).

777

778

779

780 ## Author contributions

781 Study conception and funding acquisition by SW. Experiments designed by MB and SW. Experiments
782 performed by MB, with additional data generated by CSC, AK, AJK, TEL, KWI and NJM. Refinement of
783 mitochondrial nucleic acid analysis and mitochondrial genome depletion experiments by AD. FIJI
784 macro for GAL8-mitochondrion image analysis written by LM. Time-lapse video microscopy by AW. All
785 data analysis by MB, TEL, CSC and AK. Manuscript drafted by MB and SW. Editing performed by MB,
786 NJM and SW.

787

788

789

Figures

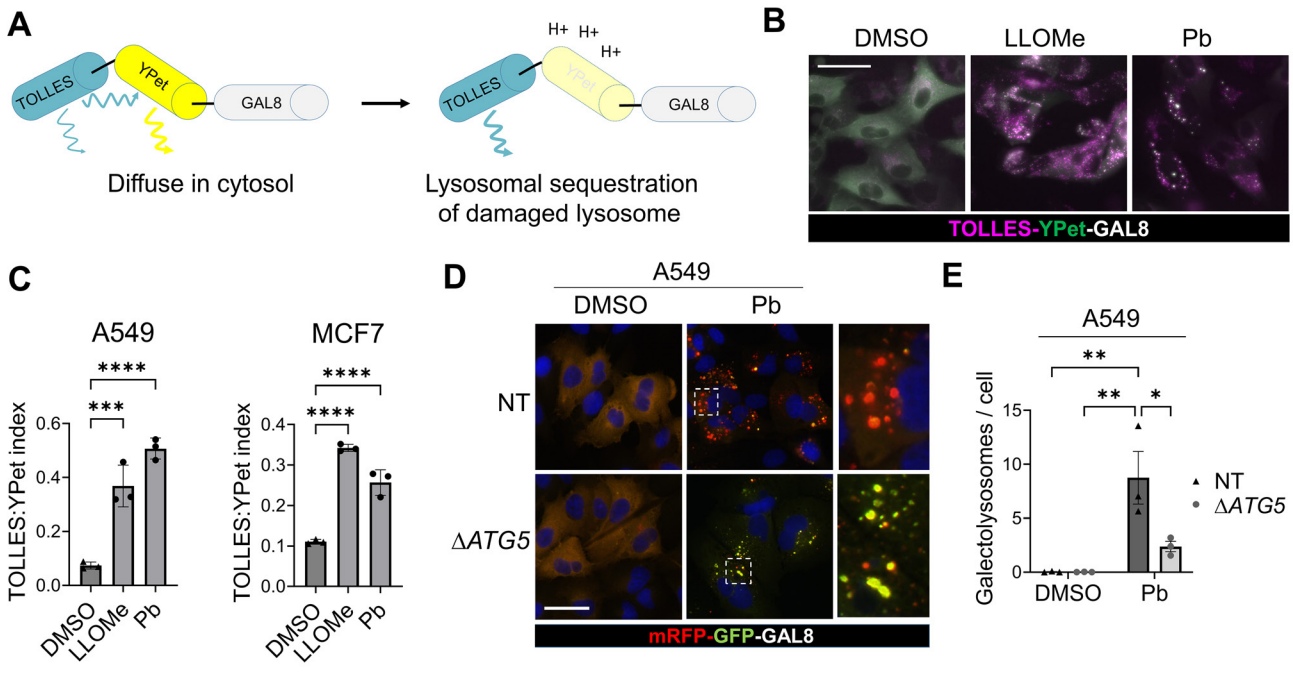

790

791

792 **Figure 1 Palbociclib induces lysophagy**

793 **A)** Schematic of SRAI (signal-retaining autophagy indicator)-Galectin 8 (GAL8) reporter for lysophagy.
794 In the cytosol, Ypet emission is low because TOLLES acts as a FRET donor. Conversely, upon completion
795 of lysophagy, Ypet is quenched by low pH and TOLLES fluorescence is apparent.

796 **B-C)** A549- or MCF7-SRAI-GAL8 cells were treated with DMSO, 0.7 mM LLOMe or 10 µM Palbociclib
797 (Pb) for 24 h then imaged by widefield fluorescence. **B)** Representative A549 images (also see **Fig. S1**).
798 **C)** Quantifications of TOLLES:Ypet (lysophagy flux) indices (n = 3 independent replicates, mean values
799 ± s.e.m., 50-100 cells per condition per replicate, *** = $P < 0.001$, **** = $P < 0.0001$, 1-way ANOVA ,
800 Holm-Šídák comparisons vs. DMSO).

801 **D-E)** A549 NT (non-targeted) or Δ*ATG5* cells expressing mRFP-GFP-GAL8 were treated with DMSO or
802 10 µM Pb for 24 h prior to imaging by widefield fluorescence. **D)** Representative images, dotted lines
803 demarcate zoom areas. **E)** Quantifications of GFP^- $mRFP^+$ galectolysosomes (n = 3 independent
804 replicates, mean values ± s.e.m., > 90 cells per condition per replicate, ** = $P < 0.01$, * = $P < 0.05$, 2-
805 way ANOVA, Holm-Šídák comparisons).

806 Scale bars = 20 µm.

807

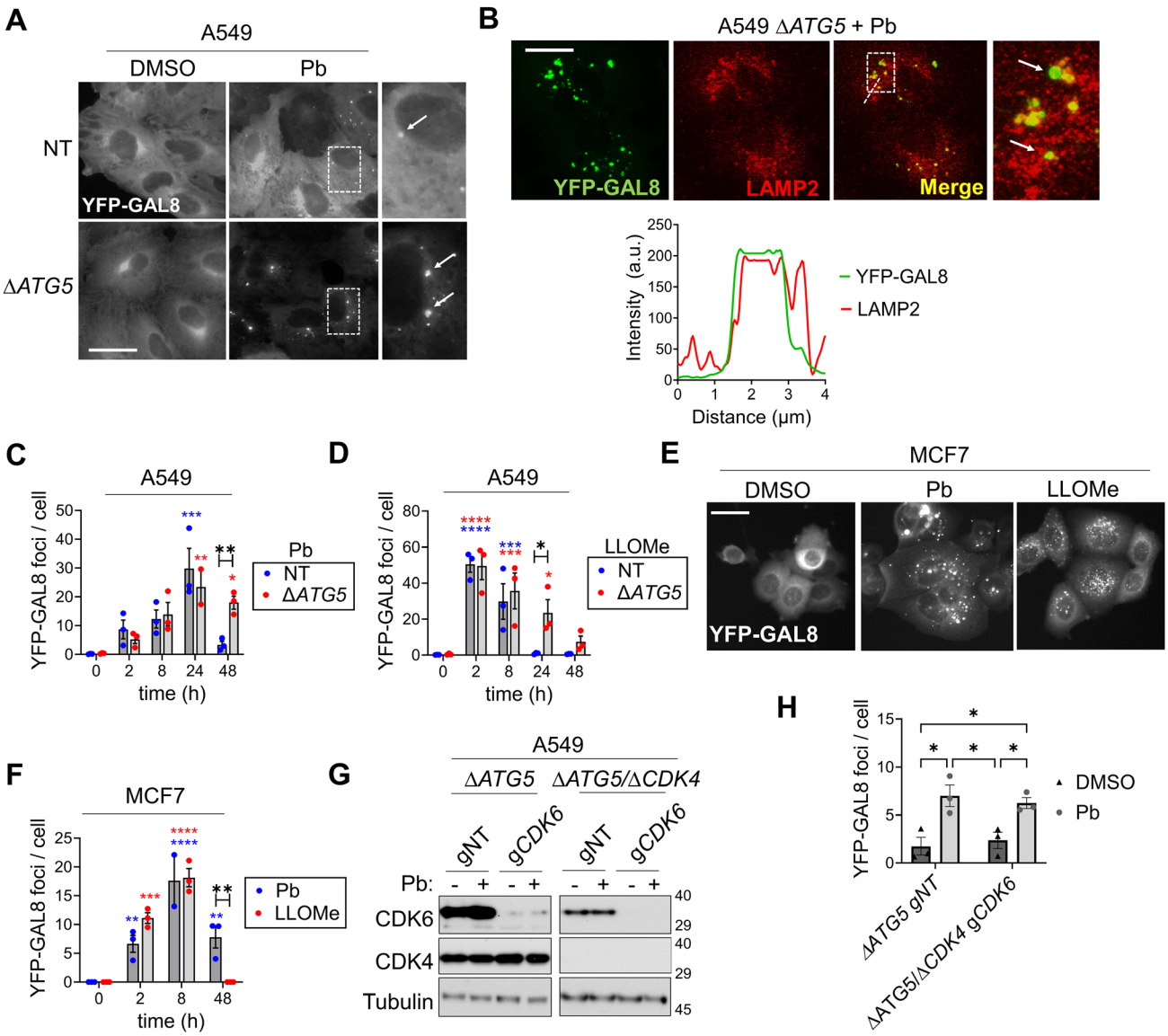

Figure 2 Palbociclib induces chronic lysosome damage

A-B) A549 NT or Δ*ATG5* cells expressing YFP-GAL8 were treated with DMSO or 10 μM Pb for 48h. **A)** Representative widefield images, dotted lines demarcate zoom areas, arrows indicate foci. **B)** Representative confocal fluorescence images of LAMP2 co-staining, arrows indicate co-localisation foci in zoom area, dotted line delineates the intensity trace (below).

C-F) A549 NT, A549 Δ*ATG5* cells and MCF7 cells expressing YFP-GAL8 were treated for indicated time points with 10 μM Pb or 0.7 mM LLOMe, prior to imaging by widefield fluorescence. YFP-GAL8 foci quantifications are presented in **C), D)** and **F)** (n = 3 independent replicates, mean values ± s.e.m., > 100 cells per condition per replicate, **** = $P < 0.0001$, *** = $P < 0.001$, ** = $P < 0.01$, * = $P < 0.05$, coloured asterisks indicate significance vs. 0 h for a given treatment, black asterisks indicate

821 significance between different treatments, mixed-effects analysis, Holm-Šídák comparisons).
822 Representative images of MCF7 cells at 24 h shown in **E)**.

823 **G-H)** A549 Δ*ATG5* cells or Δ*ATG5* Δ*CDK4* derivatives, stably expressing Cas9 and YFP-GAL8, were
824 transduced with non-targeting sgRNA (gNT) or g*CDK6*. 72 h post gRNA transduction, cells were treated
825 with DMSO (-) or 10 μM Pb (+), for 24 h and either **G)** immunoblotted or **H)** fixed for widefield
826 fluorescence microscopy quantification of YFP-GAL8 foci, comparing *CDK4/6* intact controls (Δ*ATG5*
827 gNT) with *CDK4/6* double knockout cultures (Δ*ATG5*/gΔ*CDK4* g*CDK6*) (n = 3 independent replicates,
828 mean values ± s.e.m., > 110 cells per condition per replicate, ** = $P < 0.01$, * = $P < 0.05$, 2-way ANOVA,
829 Holm-Šídák comparisons).

830 Scale bars = 20 μm.

831

832

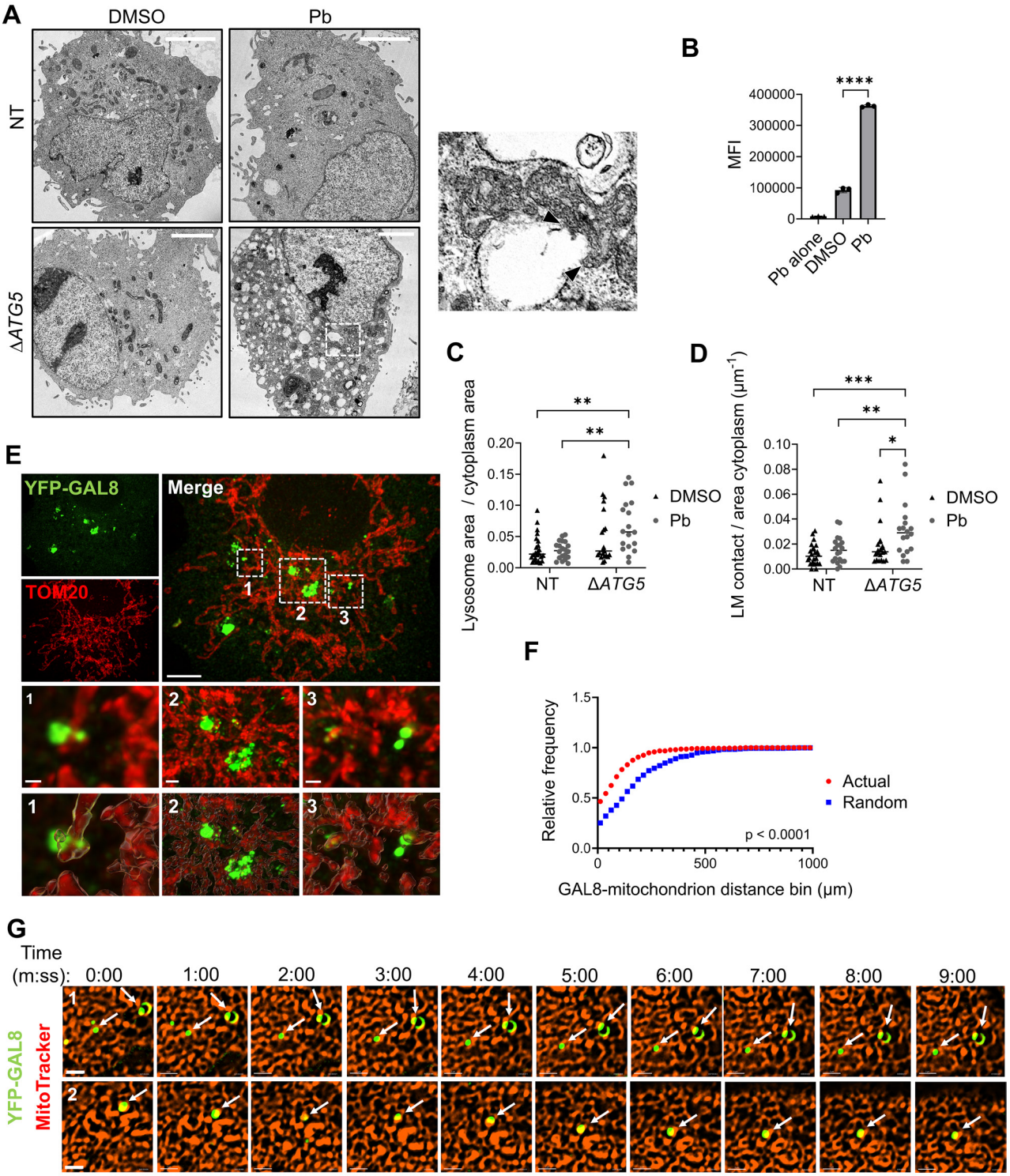

833

834

835 **Figure 3 Damaged lysosomes are associated with the mitochondrial network**

836 **A)** A549 NT (non-targeted) or Δ*ATG5* cells were treated with DMSO or 10 μM Palbociclib (Pb) for 48 h
837 then analysed by TEM, representative images shown here (*n* = 20 images per condition). Dotted lines
838 delineate a zoom area showing swollen lysosomes contacting mitochondria (arrowheads delimit a
839 contact site, defined as continuous membrane opposition of < 30 nm).

840 **B)** Δ*ATG5* A549 treated with DMSO or 10 μM Pb for 24 h were incubated for 30 min with Lysotracker
841 Red (LTR, 50 nM) (no LTR in case of Pb alone control). Lysosomal content was analysed by flow
842 cytometry and median fluorescence intensity (MFI) was quantified. (n = 3 independent replicates,
843 mean ± s.e.m., **** = $P < 0.0001$, two-tailed t-test vs DMSO).

844 **C-D)** Quantifications of TEM shown in **A)**. **C)** The proportional cross-sectional area of lysosomes within
845 the cytoplasm. **D)** The length of lysosome-mitochondria (LM) contact sites per unit area of cytoplasm
846 (n = 20 images, * = $P < 0.05$, **= $P < 0.01$, *** = $P < 0.001$, 2-way ANOVA, Holm-Šídák comparisons).
847 Scale bars, 0.5 μm.

848 **E-F)** A549 Δ*ATG5* cells expressing YFP-GAL8 were treated with 10 μM Pb for 24 h, then stained for
849 TOM20 (mitochondrion) and imaged by Super Resolution Optical Photon Reassignment Microscopy
850 (SoRA). **E)** Representative raw images in upper panels, dotted lines (1-3) delineate the zoom areas in
851 the row below and the cognate mitochondrial surface rendered images in the bottom row. **F)** Relative
852 frequency distribution of distances between YFP-GAL8 foci and rendered mitochondria (Actual),
853 compared with *in silico* shuffling of these foci within the cytoplasm (Random) (n = 400 measurements
854 from 5 cells, Kolmogorov-Smirnov test, $P < 0.0001$, representative of 3 independent experiments). See
855 also **Movie S1**. Scale bars, 5 μm (merge), 1 μm (zooms).

856 **G)** A549 Δ*ATG5* cells expressing YFP-GAL8 were treated with 10 μM Pb for 6 h, then MitoTracker-Red
857 added 30 mins prior to super-resolution radial fluctuation (SRRF) processing-facilitated time-lapse
858 microscopy. White arrows: YFP-GAL8 positive membranes associated with the mitochondrial network.
859 See also: **Movies S2, 3**. Scale bars, 2 μm. Representative of n = 4 movies (technical replicates).

860

861

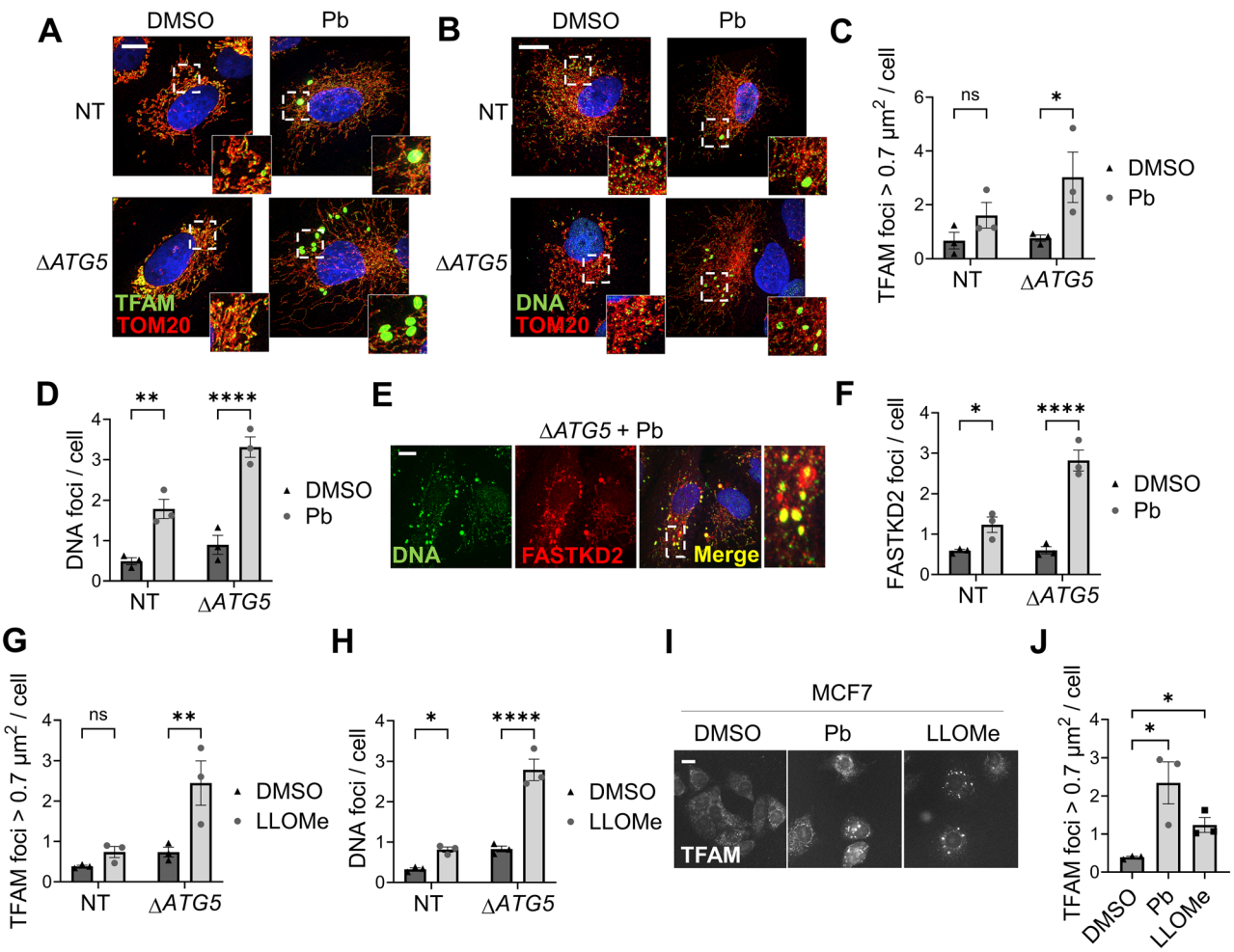

Figure 4 Lysosome damage is associated with stereotypical mitochondrial nucleic acid stress markers

A-F) A549 NT (non-targeting wild-type) or Δ*ATG5* cells were treated with DMSO or 10 μM Palbociclib (Pb) for 48 h. Cells were stained for mitochondria (TOM20) and mitochondrial nucleoids using **A,C)** anti-TFAM; **B,D)** anti-DNA; **E,F)** anti-FASTKD2 antibodies. **A,B)** Representative SoRA and **E)** confocal microscopy images. **C-D,F)** Wide-field fluorescence microscopy was used to quantify the aggregated nucleoids (TFAM foci with > 0.7 μm^2 cross-sectional area or prominent DNA/FASTKD2 foci) (n =3 independent replicates, mean values ± s.e.m., > 250 cells per condition per replicate, ns = non-significant, * = $P < 0.05$, **= $P < 0.01$, **** = $P < 0.0001$, 2-way ANOVA, Holm-Šídák comparisons DMSO vs. Pb). Dotted lines delineate zoom areas.

G-H) A549 NT or Δ*ATG5* cells were treated with DMSO or 700 μM LLOMe for 24 h. Cells were analysed for aggregated mitochondrial nucleoids as in **A)-F)**, quantifications presented here (n = 3 independent

replicates, mean values ± s.e.m, > 220 cells per condition per replicate, ns = non-significant, * = $P < 0.05$, ** = $P < 0.01$, **** = $p < 0.0001$, 2-way ANOVA, Holm-Šídák comparisons DMSO vs. LLOMe).

I-J) MCF7 cells were treated with DMSO, 700 μM LLOMe or 10 μM Pb, for 24 h, then analysed for aggregated TFAM-positive nucleoids as in **A)** and **C). I)** Representative widefield fluorescence images. **J)** Quantifications (*n* = 3 independent replicates, mean values ± s.e.m, > 150 cells per condition per replicate, * = $P < 0.05$, two-tailed t-tests vs. DMSO).

Scale bars, 10 μm.

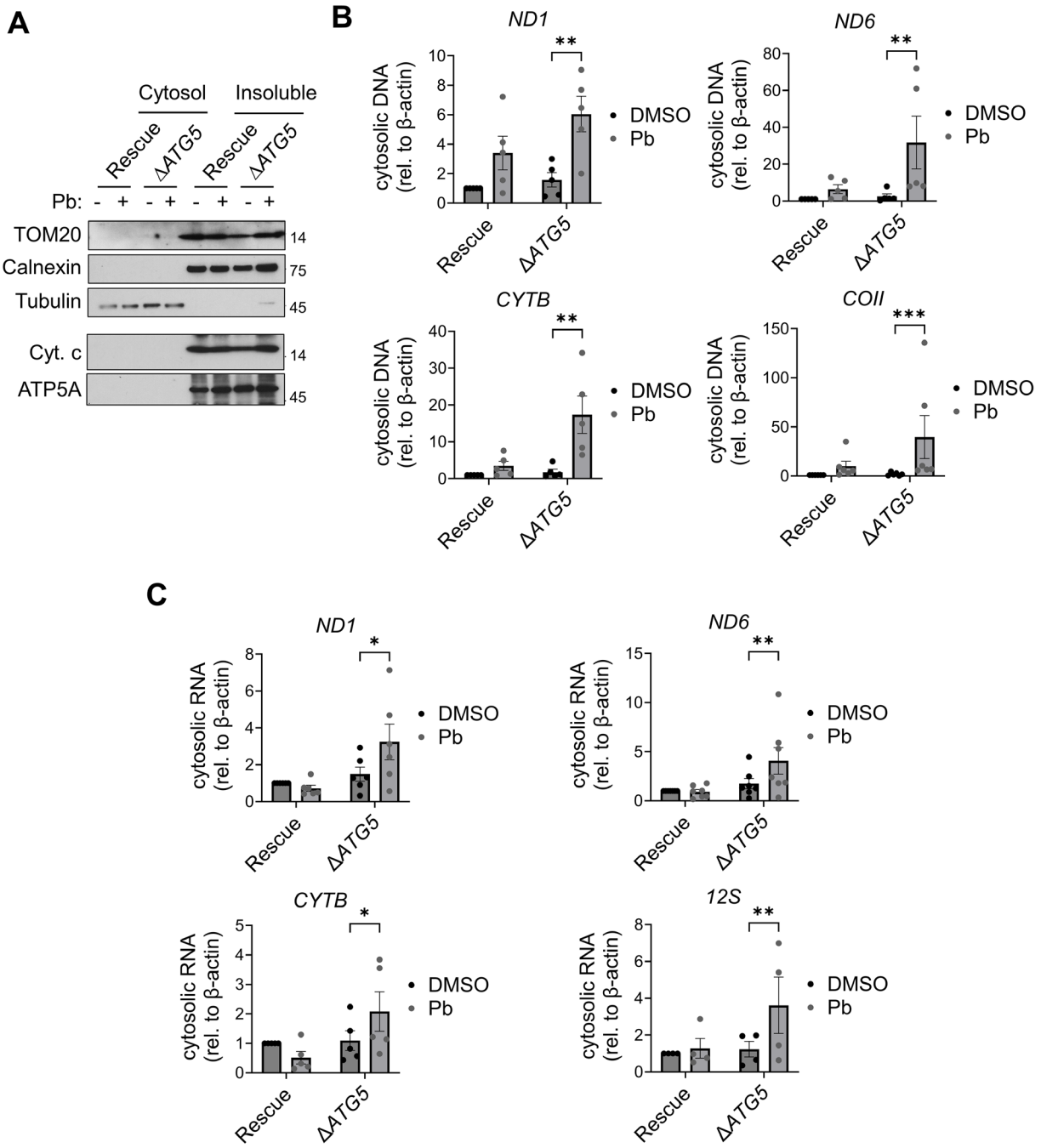

Figure 5 Mitochondrial nucleic acids are released into the cytosol by Palbociclib

A) A549 Rescue (Δ*ATG5* + GFP-*ATG5*) and Δ*ATG5* cells were treated with DMSO (-) or 10 μM Palbociclib, Pb (+), for 48 h. Pure cytosolic fraction (Cytosol) was separated from remaining cellular material including mitochondria (Insoluble) using digitonin extraction and immunoblotted to confirm purity (mitochondrial markers: TOM20; Cytochrome C; ATP5A, ER marker: Calnexin). Cytochrome C and ATP5A are from a second immunoblot on same samples from the same replicate. Representative of *n* = 3 independent replicates.

893 **B-C)** Nucleic acids (**B**, DNA; **C**, RNA) were isolated from the cytosolic fraction and qPCR performed for
894 mitochondrial genes *ND1*, *ND6*, *CYTB* and *COII*, normalised to *ACTB* from whole cell DNA (n = 4
895 independent replicates, minimally, after outliers removed by Grubb's test, mean ± s.e.m.,
896 normalisation to Rescue + DMSO, ** = $P < 0.01$, *** = $P < 0.001$, two-tailed ratio paired t-tests).

897

898

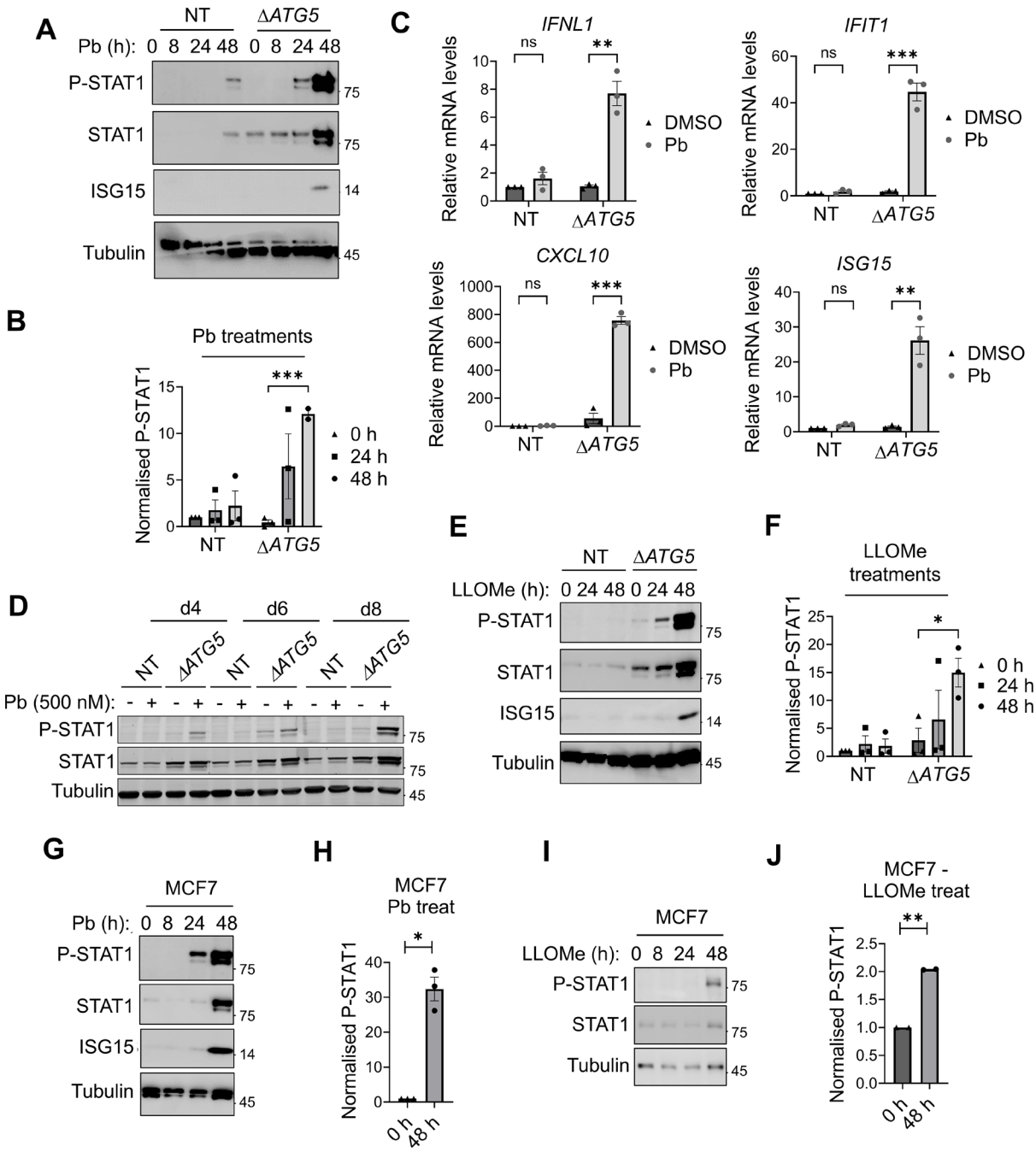

Figure 6 Chronic lysosome damage triggers interferon responses

A-B) A549 NT (non-targeted wild-type) or Δ*ATG5* cells were treated with 10 μM Palbociclib (Pb) for the indicated time and then immunoblotted for interferon pathway activation (phospho-Y701 STAT1, P-STAT1, and ISG15). **A)** Representative blot. **B)** Quantifications (n = 3 independent replicates, mean ± s.e.m., outlier removed by Grubb's test, *** = $P < 0.001$, 2-tail t-tests vs. 0 h, Holm-Šídák correction).

C) A549 NT or Δ*ATG5* cells treated as in **A** and subjected to qRT-PCR for indicated genes (n = 3 independent replicates, mean ± s.e.m., relative to *18S*, normalised to NT + DMSO, ns = non-significant, ** = $P < 0.01$, *** = $P < 0.001$, 1-sample t-test for NT, 2-tailed t-test for Δ*ATG5*).

908 **D)** A549 Δ*ATG5* cells were treated with DMSO (-) or 500 nM Pb (+), for the indicated number of days
909 (d), then immunoblotted for P-STAT1 (*n* = 3 independent replicates, representative replicate shown).

910 **E-F)** A549 NT (non-targeted wild-type) or Δ*ATG5* cells were treated with 700 μM LLOMe for the
911 indicated times then immunoblotted for interferon pathway activation (P-STAT1, ISG15). **E)**
912 Representative blot. **F)** Quantifications (*n* = 3 independent replicates, mean ± s.e.m., * = $P < 0.05$, 2-
913 tail t-tests vs. 0 h, Holm-Šídák correction).

914 **G-J)** MCF7 cells were treated with 10 μM Palbociclib (Pb) (**G**-**H**) or 700 nM LLOMe (**I**-**J**) for the indicated
915 times then immunoblotted as shown. **G,I)** Representative blots. **H,J)** Quantifications (*n* = 3
916 independent replicates, mean ± s.e.m., * = $P < 0.05$, ** = $P < 0.01$, 1-sample t-tests).

917

918

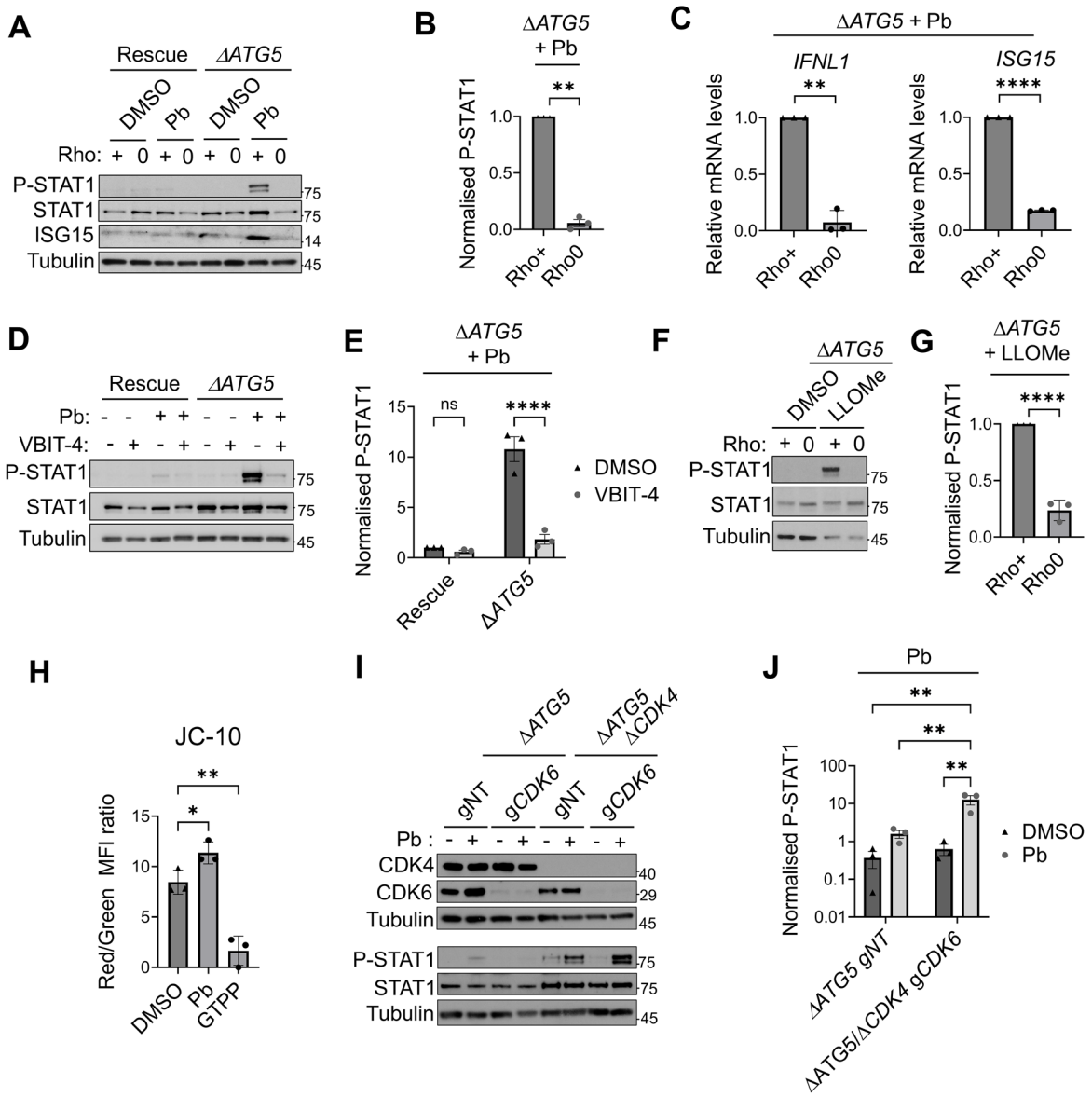

Figure 7 Mitochondrial nucleic acids are required for interferon responses associated with chronic lysosome damage

A-C) A549 Rescue (Δ*ATG5* + GFP-*ATG5*) and Δ*ATG5* cells were treated to generate control (Rho+, +) or mitochondrial genome depleted (Rho0, 0) cells. Cells were treated with DMSO or 10 μM Palbociclib (Pb) for 48 h and immunoblotted for interferon activation (phospho-Y701-STAT1, P-STAT1, ISG15). **A)** Representative blot. **B)** Quantification for Pb-treated Δ*ATG5* cells (n = 3, mean ± s.e.m., normalised to Rho+, ** = $P < 0.01$, ns = non-significant, 1-sample t-test).

C) A549 Δ*ATG5* cells (Rho+ or Rho0) were treated with 10 μM Pb for 48 h and qRT-PCR performed for *IFNL1* and *ISG15* (n = 3 independent replicates, mean ± s.e.m., relative to *18S*, normalised to Rho+, ** = $P < 0.01$, **** = $P < 0.0001$, 1-sample t-tests).

930 **D-E)** A549 Rescue or Δ*ATG5* cells were treated with DMSO or 10 μM Pb +/- 15 μM VBIT-4, then
931 immunoblotted as shown. **D)** Representative blot. **E)** Quantification for Pb-treated Δ*ATG5* cells (*n* = 3
932 independent replicates, mean ± s.e.m, ns = non-significant, **** = *P* < 0.0001, 2-way ANOVA, Holm-
933 Šídák comparisons DMSO vs. VBIT-4).

934 **F-G)** A549 Δ*ATG5* cells, Rho+ (+) or Rho0 (0), were treated with DMSO or 700 μM LLOMe for 48 h, then
935 immunoblotted for P-STAT1. **F)** Representative blot. **G)** Quantification for LLOMe treated cells,
936 normalised to Rho+ (*n* = 3 independent replicates, mean ± s.e.m., **** = *P* < 0.0001, 1-sample t-test).

937 **H)** Δ*ATG5* A549 were treated with DMSO, Pb (10 μM, 24 h) or Gamitrinib TPP (GTPP, 20 μM, 4 h). Cells
938 were then incubated for 30 min with JC-10 (15 μM) prior to analysis by flow cytometry. Quantitative
939 fluorescent ratio of JC-10 (aggregating (red, em 585) versus monomeric (green, em 525)) was used to
940 assess mitochondrial membrane potential (MFI, median fluorescence intensity) (*n* = 3 independent
941 replicates, mean ± s.e.m., ** = *P* < 0.01, * = *P* < 0.05, 1-way ANOVA, Holm-Šídák comparisons vs.
942 DMSO).

943 **I-J)** A549 Δ*ATG5* cells or Δ*ATG5* Δ*CDK4* derivatives, stably expressing Cas9, were transduced with non-
944 targeting sgRNA (gNT) or g*CDK6*. 72 h post transduction, cells were treated with DMSO (-) or 10 μM
945 Pb (+) for 24h, then immunoblotted as shown. **I)** Representative blot. **J)** Quantifications comparing
946 CDK4/6 intact controls (Δ*ATG5* gNT) with CDK4/6 double knockout cultures (Δ*ATG5*/Δ*CDK4* g*CDK6*) (*n*
947 = 3 independent replicates, mean ± s.e.m., ** = *P* < 0.01, 2-way ANOVA, Holm-Šídák comparisons).

948

949

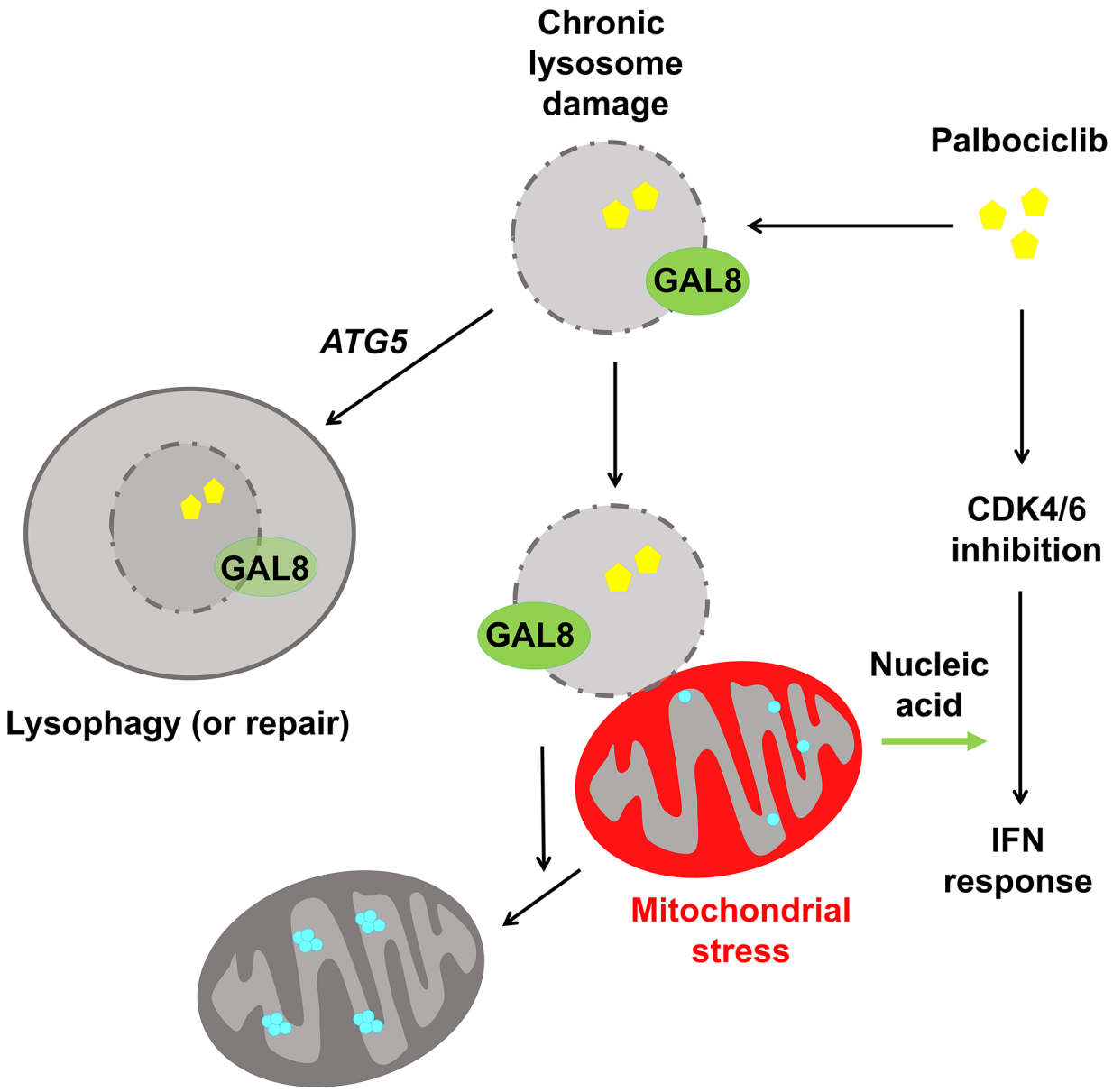

950

951 **Figure 8 Model for response to chronic lysosome damage invoked by Palbociclib**

952 See text for details. GAL8 = galectin 8. IFN = interferon. Blue dots depict mitochondrial nucleoids.